

Consistency Between the Luminosity Function of Resolved Millisecond Pulsars and the Galactic Center Excess.

Harrison Ploeg^a Chris Gordon^a Roland Crocker^b Oscar Macias^c

^aDepartment of Physics and Astronomy, Rutherford Building, University of Canterbury, Private Bag 4800, Christchurch 8140, New Zealand

^bResearch School of Astronomy and Astrophysics, Australian National University, Canberra, Australia

^cCenter for Neutrino Physics, Department of Physics, Virginia Tech, Blacksburg, VA 24061, USA

Abstract. Fermi Large Area Telescope data reveal an excess of GeV gamma rays from the direction of the Galactic Center and bulge. Several explanations have been proposed for this excess including an unresolved population of millisecond pulsars (MSPs) and self-annihilating dark matter. It has been claimed that a key discriminant for or against the MSP explanation can be extracted from the properties of the luminosity function describing this source population. Specifically, is the luminosity function of the putative MSPs in the Galactic Center consistent with that characterizing the resolved MSPs in the Galactic disk? To investigate this we have used a Bayesian Markov Chain Monte Carlo to evaluate the posterior distribution of the parameters of the MSP luminosity function describing both resolved MSPs and the Galactic Center excess. At variance with some other claims, our analysis reveals that, within current uncertainties, both data sets can be well fit with the same luminosity function.

Keywords: Galactic Center, Gamma Rays, Millisecond Pulsars

Contents

1	Introduction	1
1.1	Plan of paper	4
2	Methods	4
2.1	Modeling a Population of Millisecond Pulsars	4
2.2	Markov Chain Monte Carlo	7
3	Results	10
3.1	Spherically Symmetric Bulge	10
3.2	X-shaped Bulge	16
4	Discussion	21
5	Conclusions	28
A	Supplementary Material	28
A.1	Computational Methods	28
A.2	Resolved MSP Data	31

1 Introduction

An extended γ -ray source has been found [1–12] in the *Fermi* Large Area Telescope (*Fermi*-LAT) data covering the central $\sim 10^\circ$ of the Milky Way. This Galactic Center Excess (GCE) signal has a spectral peak at about 2 GeV and reaches a maximum intensity at the Galactic Center (GC) from where it falls off radially like $\propto r^{-2.4}$. Given its morphological and spectral characteristics, the GCE might constitute the indirect signature of the self-annihilation of dark matter particles distributed in a Navarro-Frenk-White (NFW) like density profile.

However, recent statistical studies [13–15] may have uncovered, as dim clusters of photons, a population of unresolved, point-like sources in the GCE γ -ray signal. These studies thus suggest, contrary to the dark matter hypothesis, that the GCE is actually attributable to many dim, unresolved point sources, presumably of stellar origin (though note it has also been argued that the photon clusters are merely due to variations in the gamma-ray flux associated with the small scale structure of the diffuse Galactic emission [16]). A natural explanation of these γ -ray sources (were they real and of stellar origin) is that they are millisecond pulsars (MSPs) [3, 5, 17, 18] and/or young pulsars [19] which both have GeV-peaked gamma-ray spectra (also see [20]).

This prompts the immediate question: what is the origin of this putative MSP and/or pulsar population? The pulsar hypothesis requires relatively recent star formation given the \lesssim few Myr γ -ray lifetimes of ordinary pulsars. Such star formation is absent from most of the bulge except in the $r \lesssim 100$ pc nuclear region; a young pulsar explanation of the GCE thus requires that the bulge be populated with pulsars that are launched out of the nucleus. It has been claimed that this can be achieved rather naturally by the pulsar’s natal kicks [19]. On the other hand, MSPs can be generated (in a number of ways: see below) from old stellar populations. Rather generically, two broad classes of bulge stellar population might be at play here: the bulge field stars or the bulge stars that were born in high redshift globular clusters that have been accumulated into the inner Galaxy by dynamical

friction and disrupted by tidal forces over the lifetime of the Milky Way [21]. Note that while the fraction of the bulge stellar population that derives from disrupted globular cluster is only at the \sim few percent level [22], observationally, globular cluster environments are orders of magnitude more efficient per unit stellar mass at producing MSPs [23] than field stellar populations.

A number of arguments [24–26] have been raised against MSP explanations for the GCE, the most important being:

1. It has been argued that, in the process of being spun up to millisecond (ms) periods by accretion from a binary companion, an MSP progenitor system will experience a low-mass X-ray binary (LMXB) phase and that, given there is a necessary connection between the LMXB and MSP phases, the same relative numbers of LMXB to MSPs should be seen in the GC and bulge as in other environments. However, the ratio of LMXBs to putative MSPs is much smaller for the GCE region than, for instance, globular cluster environments [26, 27].
2. It has been argued that the efficiency with which a given stellar mass of (putative) disrupted bulge globular clusters would have to be converted into MSPs is implausibly higher than the efficiency with which extant globular clusters generate γ -ray MSPs [24].
3. It has been argued that the luminosity distribution of an MSP population whose unresolved, lower-luminosity members might plausibly explain the apparently diffuse GCE signal is inconsistent with the luminosity distribution of more local (Galactic disk), resolved γ -ray MSPs [25]. In particular, it has been claimed that *Fermi* should detect many more bright MSPs from the vicinity of the GC/bulge were an MSP population to explain the GCE, whereas it detects none.

In this paper we will deal mostly with point 3. Before addressing this below, however, we take the opportunity here to explain that neither points 1 or 2 constitutes a watertight criticisms of the MSP scenario.

With respect to point 1, first note that different evolutionary pathways leading to the formation of MSPs have been proposed [28, 29], that, globally, the relative importance of these pathways is unclear, and that different pathways may have different relative importance in different stellar environments. In particular, much of the discussion to date regarding the plausibility of an MSP scenario to explain the GCE signal has implicitly adopted the ‘recycling’ scenario for MSP creation [30] where an old neutron star accretes material from a binary companion (which is either congenital or dynamically captured) and is spun up to ms periods.

However, other paths to the formation of MSPs exist and these remain entirely plausible from a theoretical perspective and not excluded by any data. For instance, MSPs may be formed via the accretion induced collapse (AIC) of a massive (close to M_{Chandra}) O-Ne-Mg white dwarf accreting from a (typically low mass) companion in a tight binary [28, 31–36]. In such systems, conservation of angular momentum in the collapse from white dwarf to neutron star results directly in a \sim ms period remnant and flux conservation naturally leads to a final neutron star field of $\sim 10^8$ G in felicitous agreement with that required by observations¹. No LMXB phases is thus necessary *before* the MSP emerges in this scenario. Mass loss (to the gravitational binding energy of the neutron star) incurred by the remnant during AIC may lead to orbit widening and an interruption to accretion. It is possible that accretion from the binary companion may be reestablished but it is also possible that winds from

¹ Another nice property of AIC-derived MSPs is that they are not expected to receive anything like as hefty a natal kick as that delivered to neutron stars resulting from core-collapse supernovae [37]. This may help to explain how so many MSPs can accumulate in globular clusters [38] – and perhaps in the inner bulge too – despite their shallow gravitational potentials.

the nascent neutron star may sufficiently ablate the companion and/or the orbital separation increased to such an extent that accretion is not reestablished [32, 36] so that an LMXB phase never occurs.

Moreover, another plausible formation channel for (individual) MSPs is merger induced collapse (MIC) of two white dwarfs. In this case there will certainly be no remaining binary companion after MIC and hence no LMXB phase [38].

In any case, even for AIC channels that lead to the formation of MSPs and subsequently undergo an LMXB phase, the relationship between the number of MSPs and the number of extant LMXBs may be quite different in the AIC scenario from the recycling scenario given the duration of the typical LMXB phases for these pathways may also be different. In summary, the uncertainty concerning which channel might dominate GC and bulge MSP creation means that the number of GC and bulge LMXBs cannot reliably be used as an indicator of the number in this region.

With respect to point 2, note that this argument only pertains in the case that the bulge MSP population putatively responsible for the GCE does derive from globular clusters; as remarked above, it might instead derive from bulge field stars (and these might produce MSPs with a different efficiency and through a different dominant channel than in the local disk). Indeed, recently there have been indications that the GCE is not spherically symmetric [39] and that it is, in fact, spatially correlated with both the X-shaped stellar over-density in the Galactic bulge and the nuclear stellar bulge [40]. This finding would seem to militate against both the young pulsar scenario and the disrupted globular cluster scenarios because there does not seem to be any good reason that pulsars kicked out of the nucleus or MSPs delivered out of disrupted globular clusters should end up in such an X-shaped distribution².

Finally, with respect to point 3, note that it has been claimed [24] that the observed γ -ray luminosity distributions of the globular cluster and the field MSP populations are similar³. Thus, were it true that disrupted globular clusters were the only plausible source of an MSP population that could supply the GCE and were point 3 above also true, this would seem to rule out the MSP scenario. However, we will argue below that, contra point 3, given the size of current uncertainties, the luminosity distributions of disk and putative GCE MSPs are perfectly consistent with each other. In addition, as we have already noted, this population need not necessarily derive from disrupted globular clusters (and, indeed, this scenario seems to be precluded by other considerations).

Given this, a putative MSP population that is responsible for the GCE presumably derives from the bulge field stars. This is a stellar population quite different from that of the local disk. In particular, the vast majority of Galactic bulge (excluding the nucleus) stars are $\gtrsim 8$ Gyr old [42] whereas the Galactic disk environment has experienced star formation up to the present day. This difference may well mean that the stellar progenitors of the putative GCE region MSPs are systematically older than the progenitors of local MSPs (and, indeed, that the MSP population is systematically older and dimmer given that MSPs spin down and become less luminous over time). There is then no strong reason to expect that the luminosity distributions of the local disk and the GCE region are the same because the stellar populations of these environments are quite different.

To this it may be objected that the stellar populations of MSP-hosting globular clusters are at least as old as the stars in the bulge. However, globular clusters' typically much higher stellar densities may render the dynamic formation of binary systems suitable for forming MSPs probable while a dynamic formation channel remains unlikely amongst the bulge field stars⁴. In summary,

²The stars that end up in the stellar X likely derive from a buckling instability induced in the early Galactic disk by the Galactic bar; see [40] and refs. therein.

³This seems somewhat in tension with the finding that globular cluster MSPs seem to spin faster and have high magnetic fields than field MSPs in the disk [41]. However, these effects may be at least partially attributable to observational biases.

⁴Likewise, while the inner ~ 200 pc of the Galaxy does experience ongoing star formation, as mentioned, its stellar

the stellar populations and environments of the local disk, the Galactic bulge, globular clusters, and the Galactic nucleus are all quite distinct; there is no logical reason to expect that the populations of MSPs formed out of these different stellar populations/environments should be identical in character, particularly in regard to their current luminosity distribution.

Equally, given the stellar populations and stellar environments of the local disk and the bulge are quite distinct, the efficiency for the production of MSPs per unit stellar mass formed may be quite different (particularly if different MSP production channels are more or less important in different circumstances).

1.1 Plan of paper

Having thus explained how the MSP scenario is by no means excluded by other considerations, in the remainder of this paper we proceed to determine the luminosity function that simultaneously describes the population of MSPs currently resolved by the *Fermi*-LAT and the putative population of MSPs that would explain the GCE. This is interesting to check as, if it were not possible to simultaneously fit both populations of MSPs with the same luminosity function as claimed by ref. [25], then this would have implications for the bulge MSP population posited to explain the GCE. To presage our main result, we have found that the GCE provides only a weak constraint on the luminosity function and that parameters can be found where both sets of data can be fit by the same luminosity function. We modeled cases where the GCE is assumed to have a spherical geometry and where it is correlated with the stellar X-bulge. In Section 2 our Bayesian Markov Chain Monte Carlo (MCMC) based approach to the problem is described. Our results are given in Section 3. Comparison to results from previous studies are discussed in Section 4 and our conclusions are given in Section 5. Some more technical aspects of our study are available in the Appendix.

2 Methods

We used 71 MSPs found within the Fermi-LAT third source catalog (3FGL) [43]. In the 3FGL, MSPs are not distinguished from pulsars and so the Galactic disk MSPs were identified by searching the Australia Telescope National Facility (ATNF) pulsar catalog [44] for 3FGL pulsars with periods of less than 10 milliseconds and which were not associated with globular clusters. A small number of additional MSPs were identified through the use of an online list and found in the 3FGL catalog⁵. The list of the MSPs that we used is given in table 6.

2.1 Modeling a Population of Millisecond Pulsars

To simulate the GCE and a population of observed MSPs to compare with data, the underlying population of MSPs must be modeled. This requires spatial and luminosity models and, for the MSPs around the GC that may be responsible for the excess, a distribution of spectra.

As in ref. [25], we used a lognormal luminosity function. The lognormal distribution is one in which the logarithm of luminosity is normally distributed, its probability density function is:

$$p(L) = \frac{1}{\sigma_L L \sqrt{2\pi}} \exp\left(-\frac{(\ln(L) - \ln(L_{\text{med}}))^2}{2\sigma_L^2}\right) \quad (2.1)$$

where L is luminosity, L_{med} is the median luminosity, and $\ln(L_{\text{med}})$ and σ_L are the mean and standard deviation of the normal distribution in $\ln(L)$.

density and extreme interstellar medium parameters mean that it is a quite different environment to the local disk. Thus even though both regions experience ongoing star formation, they are also quite different environments.

⁵<https://confluence.slac.stanford.edu/display/GLAMCOG/Public+List+of+LAT-Detected+Gamma-Ray+Pulsars>

The spatial distribution of MSPs was divided into two components. One of these components models a population of MSPs scattered throughout the Milky Way disk according to the following density distribution [45]:

$$\rho_{\text{disk}}(r_{\text{cyl}}, z, N_{\text{disk}}) = \frac{N_{\text{disk}}}{4\pi\sigma_r^2 z_0} \exp(-r_{\text{cyl}}^2/2\sigma_r^2) \exp(-|z|/z_0) \quad (2.2)$$

where r_{cyl} is the distance from the GC projected onto the Galactic plane, z is the distance perpendicular to the Galactic plane, N_{disk} is the total number of MSPs in the entire Galactic disk, and σ_r and z_0 are scale parameters. We take the distance from us to the GC to be 8.25 kpc.

The second component of the spatial distribution models the bulge population of MSPs potentially contributing to the GCE. In our region of interest, this density distribution has been found to be fitted by a spherically symmetric power law profile [1–7, 9, 10, 12]. In this article we use the parameterization

$$\rho_{\text{bulge}}(r, N_{\text{bulge}}) = \frac{3N_{\text{bulge}}}{20\pi r_{\text{bulge}}^{0.6}} r^{-2.4}, \quad 0 \leq r < r_{\text{bulge}} \quad (2.3)$$

where N_{bulge} parameter is the total number of bulge MSPs in the Galaxy, r is the distance from the GC, and r_{bulge} is the maximum radial extent of the bulge. The power law index is only known to about 20% accuracy, but our results are insensitive to this variation. We used a bulge radius of $r_{\text{bulge}} = 3.1$ kpc to be consistent with ref. [25]. This is also the value determined from the COBE-DIRBE NIR maps [46].

In addition to the spherically symmetric bulge model, an alternative model in which the bulge is X-shaped [40] was also investigated. In this case, the spatial distribution is the product of the density profiles along the principle axes as shown in figure 7 of ref. [47], but includes only points randomly generated inside the projected X-shaped structure in Galactic coordinates. This X-shaped bulge distribution is shown in figure 1.

Once the positions and luminosities of a population of MSPs (in both the disk and bulge) were simulated, an observed population could be found by applying a detection threshold based on the flux of each MSP, where the relationship between flux F , luminosity L and distance d is:

$$F = \frac{L}{4\pi d^2} \quad (2.4)$$

A resolved MSP is one for which $F \geq F_{\text{th}}$, where F_{th} is the threshold flux. The second Fermi-LAT catalog of gamma-ray pulsars [48] included an attempt to find the detection threshold as a function of l and b by adding simulated point sources at different positions in the sky and determining what the minimum flux needed was before they were detected. As the sensitivity to point sources depends strongly on the gamma-ray background, the detection threshold is highest near the Galactic plane. As in ref. [25], our modeled threshold did not solely depend on location in Galactic coordinates. Instead, F_{th} was drawn from a lognormal distribution for each simulated MSP:

$$p(F_{\text{th}}) = \frac{1}{\sigma_{\text{th}} F_{\text{th}} \sqrt{2\pi}} \exp \left[-\frac{(\ln(F_{\text{th}}) - (\mu_{\text{th}}(l, b) + K_{\text{th}}))^2}{2\sigma_{\text{th}}^2} \right] \quad (2.5)$$

where K_{th} and σ_{th} are parameters, and $\mu_{\text{th}}(l, b)$ is the natural logarithm of the threshold flux at l and b according to the pulsar catalog. A map of $2 \exp(\mu_{\text{th}}(l, b))$ is given in figure 16 of ref. [48].

The authors of ref. [48] point out that these reported detection thresholds are likely to be underestimates; K_{th} is included as a parameter to account for this. The purpose of drawing F_{th} from the lognormal distribution is to approximate the variation that may occur due to uncertainty in the estimated threshold, or characteristics specific to individual pulsars, such as their spectra or light curves.

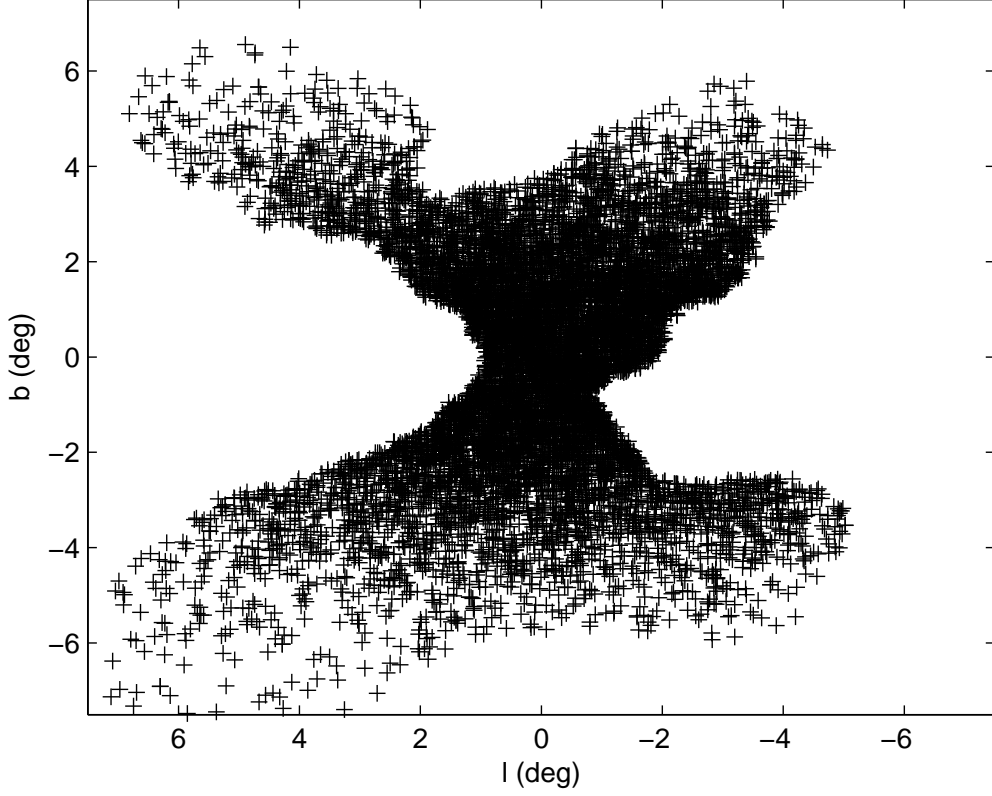


Figure 1. Simulated spatial distribution of MSPs in X-shaped bulge.

The consequence of this is that the detection probability of a pulsar increases with flux, and does so particularly rapidly around the median of the threshold distribution, $\mu_{\text{th}}(l, b) + K_{\text{th}}$.

To simulate the GCE, a distribution of spectra must be modeled for the bulge MSPs. In the 3FGL catalog sources were fitted with three different spectral shapes. One of these is a power law:

$$\frac{dN}{dE} \propto \left(\frac{E}{E_0} \right)^{-\Gamma} \quad (2.6)$$

The second is an exponentially cutoff power law:

$$\frac{dN}{dE} \propto \left(\frac{E}{E_0} \right)^{-\Gamma} \exp\left(-\frac{E}{E_{\text{cut}}}\right) \quad (2.7)$$

Finally, a log parabolic spectrum was fitted for a small number of the observed MSPs:

$$\frac{dN}{dE} \propto \left(\frac{E}{E_0} \right)^{-\omega - \beta \ln(E/E_0)} \quad (2.8)$$

Each simulated bulge MSP was assigned the spectral shape and best fit parameters of a random resolved MSP. The proportionality constant was then found by requiring the energy integral over the

spectrum (from 0.1 to 100 GeV) be equal to the flux of the simulated MSP:

$$F = \int_{0.1 \text{ GeV}}^{100 \text{ GeV}} E \frac{dN}{dE} dE \quad (2.9)$$

The simulated gamma-ray excess was then the sum of the spectra of all the MSPs in the relevant region of interest. This region is the $7^\circ \times 7^\circ$ box around the Galactic Center in the case of the spherically symmetric bulge, and for the X-shaped bulge it is the entire simulated bulge (which is inside a $15^\circ \times 15^\circ$ region).

2.2 Markov Chain Monte Carlo

In Subsection 2.1 a model was described which can produce a simulated population of MSPs, decide which are resolved, and simulate a gamma-ray excess based on the bulge MSP population. To find the parameters which may best reproduce the data, it is necessary to have a method for randomly sampling an arbitrary and potentially complex probability distribution of any number of dimensions. The adaptive Metropolis MCMC algorithm described in ref. [49] was used for this.

We used an unbinned Poisson distribution for the likelihood of the resolved MSPs [50]:

$$\mathcal{L}_{\text{res}} \propto \exp(-\lambda_{\text{res}}) \prod_{i=1}^N \rho(l_i, b_i, d_i, F_i) \quad (2.10)$$

where $N = 71$ is the number of resolved MSPs, λ_{res} is the expected number of resolved MSPs, $\rho(l_i, b_i, d_i, F_i)$ is the modeled density of resolved MSPs at Galactic coordinates l_i, b_i , distance d_i , and flux F_i .

We used the following parameters (θ):

1. The total expected number of observed MSPs λ_{res} from eq. (2.10).
2. The natural log of the ratio of total number of disk to bulge MSPs $\ln(r_{\text{d/b}}) = \ln(N_{\text{disk}}/N_{\text{bulge}})$ from eqs. (2.3) and (2.2).
3. Luminosity function parameters $\log_{10}(L_{\text{med}})$ and σ_L for the lognormal distribution given by eq. (2.1).
4. The flux threshold distribution parameters K_{th} and σ_{th} from eq. (2.5).
5. The spatial model parameters σ_r and z_0 .
6. The distance parameter for each observed MSP, d_i .
7. The parallax distance measurement probability parameter α .
8. The flux of each observed MSP, F_i .
9. The flux threshold at each observed MSP, $F_{\text{th},i}$.

Note that λ_{res} appears as a parameter (rather than being fixed to the observed number of MSPs) because the observed number is essentially drawn from a Poisson distribution with an unknown expected value. The parameters λ_{res} and σ_{th} were required to be greater than 0 and σ_L was restricted to values above 0.5. A lower limit of 0.8 for σ_L is justified in ref. [25] by considering the luminosity distribution of those MSPs with parallax distance measurements. Here, those measurements were included as priors on the distance parameters corresponding to those MSPs. The upper limit for σ_r was

10.0, this was chosen as it is expected to be approximately 5 kpc [25, 45, 51–53]. Prior boundaries were also used for other parameters, these boundaries were located in places where the likelihood was very low (i.e. the proposed set of parameters would be extremely unlikely to be accepted). Table 1 lists prior boundaries placed on each of the parameters.

Parameter	Lower Boundary	Upper Boundary
λ_{res}	0.0	-
$\ln(r_{\text{d/b}})$	-	-
K_{th}	0.0	3.9
σ_{th}	0.0	2.3
σ_r/kpc	0.0	10.0
z_0/kpc	0.0	2.0
d_i/kpc	0.0	-
$\log_{10}(L_{\text{med}}/(\text{erg} \cdot \text{s}^{-1}))$	29.0	38.0
σ_L	0.5	3.5
α/kpc	0.01	10.0
$F_{\text{th},i}/(\text{erg} \cdot \text{cm}^{-2} \cdot \text{s}^{-1})$	0	F_i
$F_i/(\text{erg} \cdot \text{cm}^{-2} \cdot \text{s}^{-1})$	$\exp(\ln(L_{\text{med}}) - 6\sigma_L)/(4\pi d_i^2)$	$\exp(\ln(L_{\text{med}}) + 6\sigma_L)/(4\pi d_i^2)$

Table 1. Prior boundaries used for each parameter in the MCMC simulation for a lognormal luminosity function.

We do not use the dispersion estimates of the MSPs distances as they may have a high systematic error [25, 48].

The expected excess that would be produced by the bulge MSPs can be found by multiplying N_{bulge} by the expected contribution of a single MSP. For the X-shaped bulge GCE data, some of the higher energy bins had large relative errors, so they were combined. The large size of the resulting bin meant that it was necessary to take $(\frac{dN}{dE})_{\text{sim},i}$ to be the mean across the bin, $N/(E_{\text{max},i} - E_{\text{min},i})$, where $E_{\text{min},i}$ and $E_{\text{max},i}$ are the edges of the bin. The highest energy bin we used in the X-bulge case was $(28 \text{ GeV} \leq E \leq 158 \text{ GeV})$. It corresponded to an expected value of around 43 counts which was the smallest value for both the spherical and X-bulge spectrum. So as the counts in each bin are reasonably high, the GCE likelihood will be well approximated [54] by a Gaussian:

$$\mathcal{L}_{\text{GCE}} \propto \prod_{i=1}^N \exp \left(- \left(\left(\frac{dN}{dE} \right)_{\text{sim},i} - \left(\frac{dN}{dE} \right)_{\text{data},i} \right)^2 / (2\sigma_{\text{data},i}^2) \right) \quad (2.11)$$

where $(\frac{dN}{dE})_{\text{sim},i}$ and $(\frac{dN}{dE})_{\text{data},i}$ are respectively the simulated and observed gamma-ray excess with uncertainty $\sigma_{\text{data},i}^2$ at E_i . This is calculated using the GCE spectra from refs. [5] and [40].

The second component of the likelihood \mathcal{L}_{res} is given by eq. (2.10) with

$$\rho(l_i, b_i, d_i, F_i) \propto (\rho_{\text{disk}} + \rho_{\text{bulge}}) p(L_i) d_i^4 \quad (2.12)$$

where $p(L_i)$ is the luminosity function given by eq. (2.1), the factor d_i^4 is from a product of a factor of d_i^2 from the Jacobian for the change of variables F_i to L_i and another factor of d_i^2 from the Jacobian for the change of variables from Cartesian to Galactic coordinates as ρ_{disk} and ρ_{bulge} are densities in Cartesian coordinates. Also, ρ_{disk} and ρ_{bulge} are determined by eqs. (2.2) and (2.3) respectively. For

our prior distribution we used:

$$p(\theta) \propto \prod_{i=1}^N p(F_{\text{th},i}) p(F_i | F_{\text{data},i}, \sigma_{\text{data},i}) \prod_{i \in \text{parallax}} p(d_i) \quad (2.13)$$

where $p(F_{\text{th},i})$ is given by eq. (2.4), $p(F_i | F_{\text{data},i}, \sigma_{\text{data},i})$ is a normal distribution with the observed MSP's flux and uncertainty (obtained from 3FGL) as the mean and standard deviation respectively and $p(d_i)$ is constructed for the subset of MSPs which had parallax measurements using the best fit value and errors.

As parallax measurements are more likely to be available for nearer MSPs, a third component of the likelihood was used. This $\mathcal{L}_{\text{parallax}}$ is the product of modeled probabilities of observed MSPs having or not having a parallax distance measurement:

$$\mathcal{L}_{\text{parallax}} = \prod_{i \in \text{parallax}} \exp(-d_i/\alpha) \prod_{i \notin \text{parallax}} (1 - \exp(-d_i/\alpha)) \quad (2.14)$$

The posterior distribution was obtained by combining the likelihood and prior distributions:

$$p(\theta | \text{data}) \propto \mathcal{L}_{\text{res}} \times \mathcal{L}_{\text{GCE}} \times \mathcal{L}_{\text{parallax}} \times p(\theta) \quad (2.15)$$

We marginalized over the $F_{\text{th},i}$ and the F_i variables using numerical integration. The other variables were sampled using the MCMC. Twelve Markov chains were constructed of five million iterations each for the spherical and X-shaped models.

Although, we have a large number of parameters that we are fitting, this is ameliorated as the flux (F_i) and distance parameters (d_i) are all linked by the geometric model (eqs. (2.2) and (2.3) or the X-bulge version) and the luminosity function given by eq. (2.1). Also, the threshold parameters ($F_{\text{th},i}$) are linked by the threshold prior giving by eq. (2.5). This regularizes the problem in a similar way to ridge regression [55].

We tested our model fits using posterior predicted p-values (see Chapter 6 of ref. [55]). For every 1250th step in the Markov chains we produced a set of simulated resolved MSPs and GCE data points. The resolved MSPs were binned in longitude, latitude, flux and distance. In order to determine if a point was well fit we evaluated the posterior predicted p-value as the fraction of simulated points of greater magnitude than the data point. The fit was considered to be acceptable if the posterior predicted p-value was between 0.025 and 0.975.

To further test our overall model fits, we randomly pick 200 parameter sets from the Markov chains, and for each of these we simulate 500 sets of resolved MSP and GCE data. We bin the resolved MSPs in l , b and $\log(F)$, we take the mean number in each bin to be the expectation value and use Poisson distributions to calculate the likelihood for the observed data as well as each set of simulated data:

$$\mathcal{L} = \prod_{i=1}^n \frac{\lambda_i^{N_i} \exp(-\lambda_i)}{N_i!} \quad (2.16)$$

where n is the total number of bins, N_i is the number of resolved MSPs in bin i with expectation value λ_i . We used 5 bins along each of l and b , and 7 along $\log(F)$ for a total of 175 bins. We can then calculate a p-value using the fraction of likelihoods for simulated data sets lower than that of the observed data. Similarly, we can also find p-values for the GCE using eq. (2.11) where $(\frac{dN}{dE})_{\text{sim},i}$ is the mean of the simulated data. The simulated data in each bin is also shifted by a random sample from a normal distribution with a standard deviation equal to the error on the observed data. The resulting distributions of p-values indicate the extent to which the distribution of model parameters in the Markov chains fits the data.

3 Results

For both the spherical and X-bulge models, corner plots are presented [56] showing the results of the MCMC simulations. These figures show histograms of the two parameters associated with the number of MSPs (λ_{res} and $\ln(r_{\text{d/b}})$), the luminosity function parameters, the flux threshold distribution parameters, the spatial parameters and the parallax model parameter. In addition to those histograms, these figures display the distributions for each pair of model parameters along with 68% and 95% contours. The distance parameters (d_i) are not shown as these were considered nuisance parameters.

To check the fit quality, for each chain, the parameters of a few thousand evenly spaced points were used to generate a simulated set of resolved MSPs. This simulated data was binned in l , b , $\log_{10}(F)$ and $\log_{10}(d)$ and the means and standard deviations of each bin are compared to the observed data in a set of figures for each model. The distribution of the simulated GCE is also plotted along with the measured data. A pair of plots are also shown which display the distribution of the number of simulated resolved MSPs both inside and outside the projected bulge region compared with the observations. The projected bulge region is all Galactic coordinates where the probability of a bulge MSP being modeled is non-zero.

We also estimated how many bulge MSPs are expected to be resolved by Fermi-LAT and future experiments with double and four times the sensitivity of the current Fermi-LAT data. We did this by evaluating, for every step in the Markov chains, the expected number of observed bulge MSPs along with the expected number for the cases where the flux thresholds were divided by factors of two and four. Using the series of expected values for each of the three cases, Poisson distributions were randomly sampled giving a discrete distribution of values N , the number of resolved bulge MSPs. From these three distributions, the overall probability for getting any N can be estimated. Histograms of these probability distributions are shown for each model along with a table showing the mean and the probability of $N > 0$.

3.1 Spherically Symmetric Bulge

In this section the results for the spherically symmetric bulge model are presented. In figure 2, the distribution of points in the set of Markov chains produced for this model is shown. Correlations can be seen between $\log_{10}(L_{\text{med}})$ and σ_L as well as between the three parameters $\ln(r_{\text{d/b}})$, K_{th} and σ_{th} . Table 2 presents the mean and error for each model parameter.

Parameter	Mean	Error
λ_{res}	73	9
$\ln(r_{\text{d/b}})$	-0.1	0.3
$\log_{10}(L_{\text{med}}/(\text{erg} \cdot \text{s}^{-1}))$	32.1	0.5
σ_L	1.4	0.3
K_{th}	2.2	0.3
σ_{th}	0.7	0.1
σ_r/kpc	6	2
z_0/kpc	0.6	0.2
α/kpc	0.43	0.09

Table 2. Mean values and 68% confidence interval errors for lognormal luminosity distribution and spherical bulge model parameters.

A set of figures show the results of using the sets of parameters in the Markov chains constructed using this model to simulate populations of MSPs. In figure 3, the binned distributions of resolved

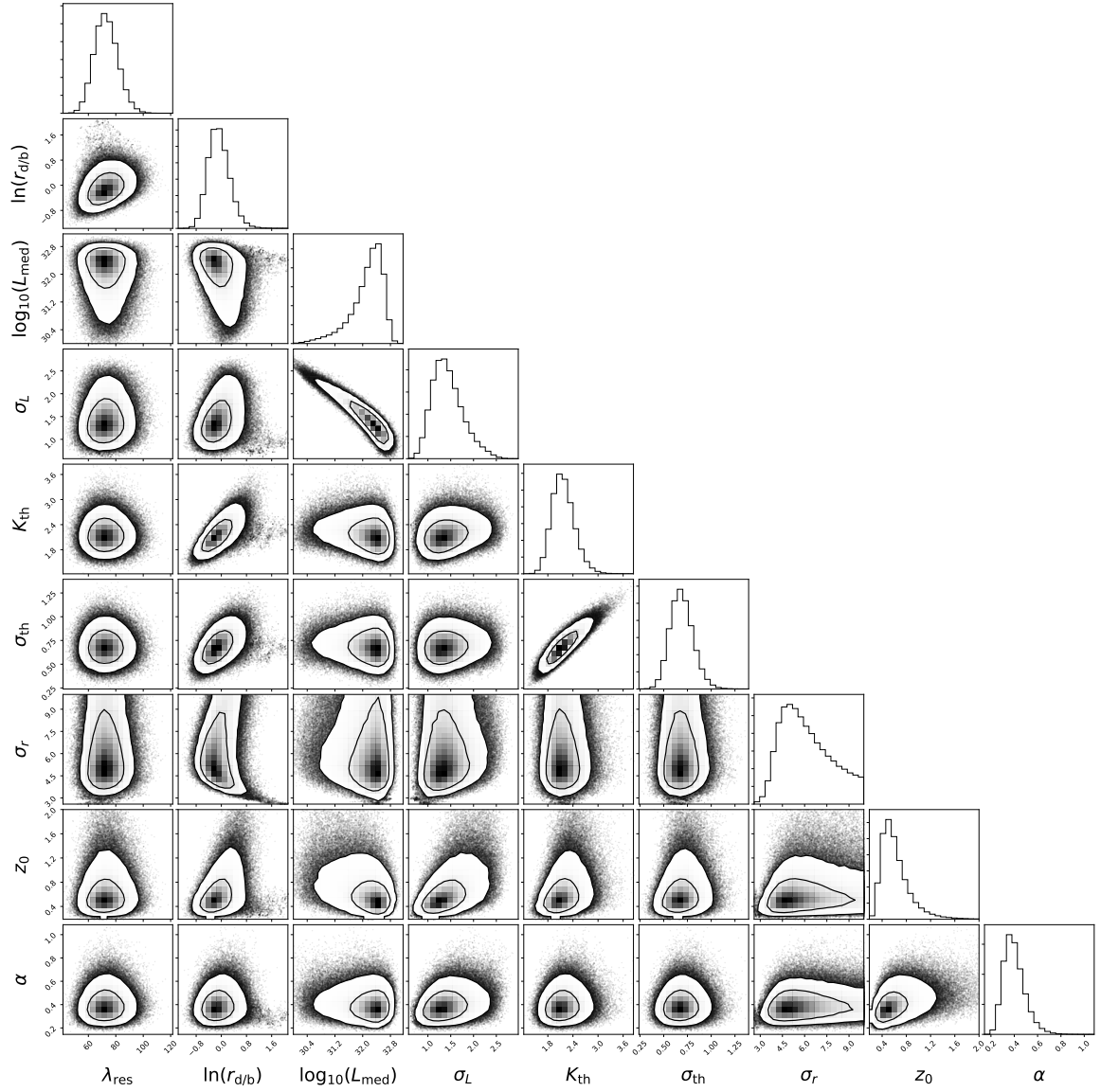


Figure 2. Distribution of points in Markov chains for the lognormal luminosity distribution and spherical bulge model. Contours contain 68% and 95% of points. The units of L_{med} and α are $(\text{erg} \cdot \text{s}^{-1})$ and kpc respectively.

MSPs in longitude, latitude, distance and flux are shown, as well as the simulated GCE produced by the bulge population. The distribution of the number of resolved MSPs inside and outside of the projected bulge region is seen in figure 4.

Table 3 shows the probability of observing any MSPs from the bulge population and the expected number based on the fitted flux threshold parameters as well as where the detection sensitivity has been doubled and quadrupled. These three probability distributions in the number of resolved bulge MSPs are shown in figures 5 and 6. The number of MSPs in the disk with luminosity greater than $10^{32} \text{ erg} \cdot \text{s}^{-1}$ was $(4 \pm 2) \times 10^4$ and the number in the bulge was $(4.0 \pm 0.9) \times 10^4$. In figure 7, the distributions of the number of MSPs are shown.

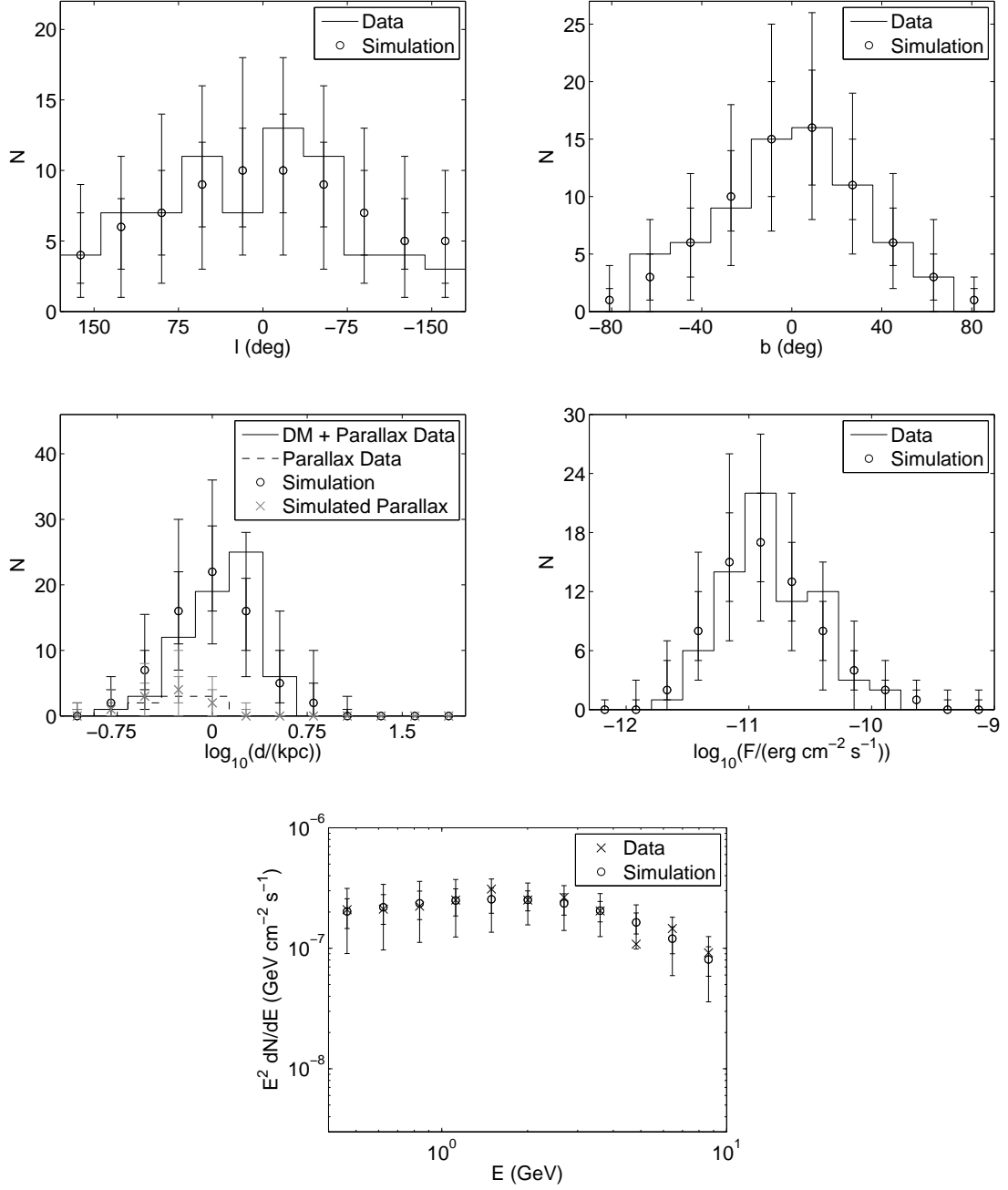


Figure 3. Simulated observed distribution of MSPs in longitude, latitude, distance and flux, and simulated GCE for the spherical bulge model and lognormal luminosity function. In the distance plot, DM means dispersion measure derived distances. The simulated points and error bars are the median, 68% and 95% intervals of the simulated populations in each bin. The error bars on the simulated GCE include the errors on the observed data.

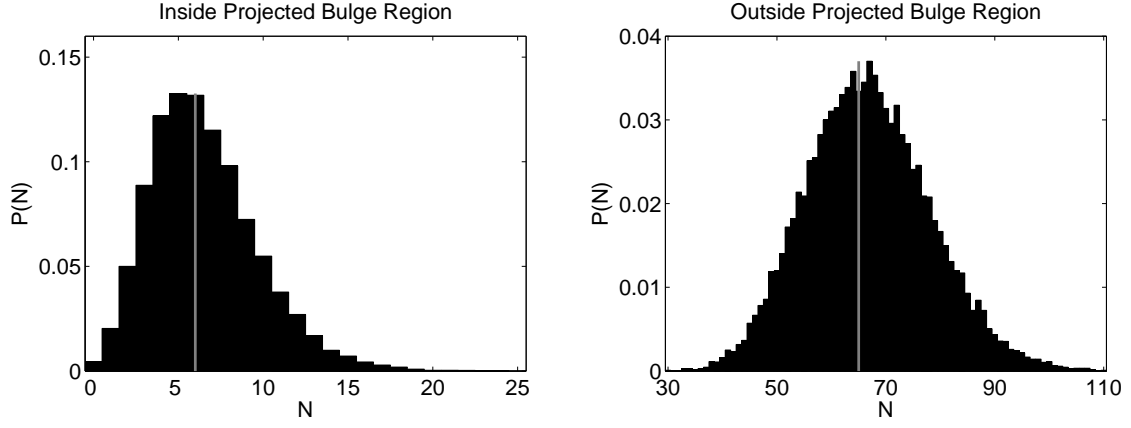


Figure 4. The approximate probability distributions of observing N MSPs inside and outside the projected bulge using the lognormal luminosity distribution and spherical bulge model. Here the projected bulge region is anywhere within 21.3° of the GC. The gray lines are the observed number for each case.

Sensitivity Factor	Mean N	$P(N > 0)$
1.0	1.42	0.577
2.0	6.81	0.917
4.0	30.1	0.997

Table 3. Expected number of observed MSPs located in the bulge and probability of observing one or more for lognormal luminosity distribution and spherical bulge model. The sensitivity factor is the number of times more sensitive the prediction is than the current data.

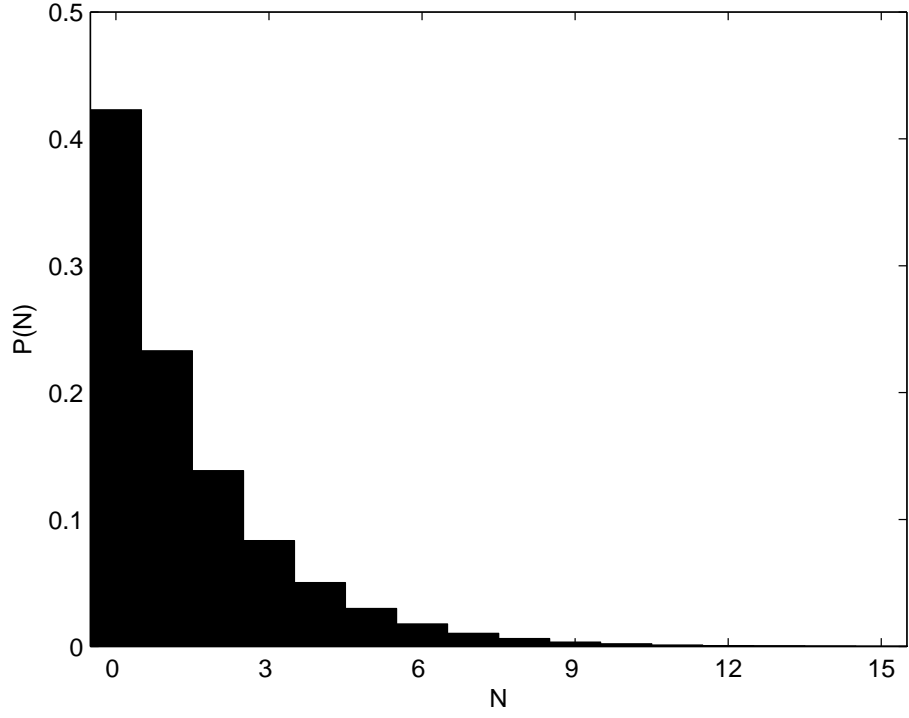


Figure 5. The probability distribution of observing N MSPs from the bulge population based on the spherical bulge model and lognormal luminosity function.

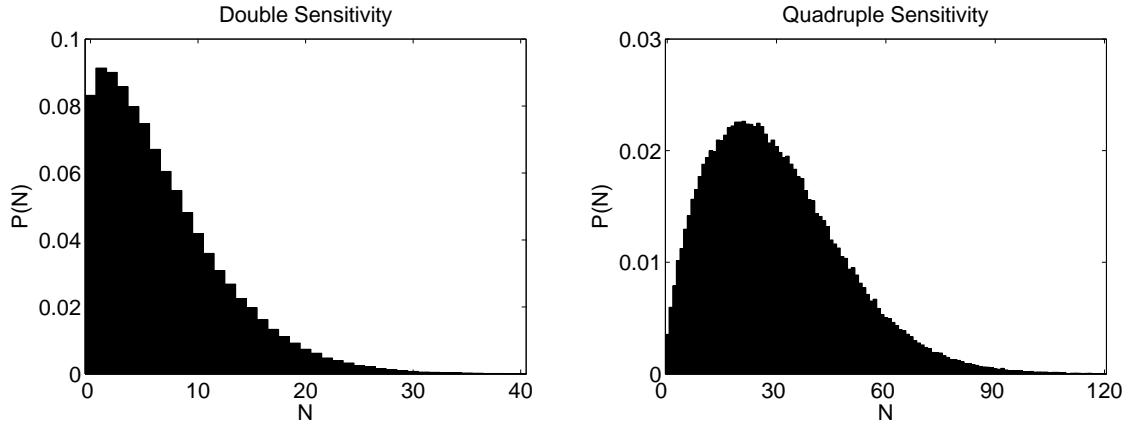


Figure 6. The probability distribution of observing N MSPs from the bulge population based on the lognormal luminosity distribution and spherical bulge model with double or quadruple sensitivity.

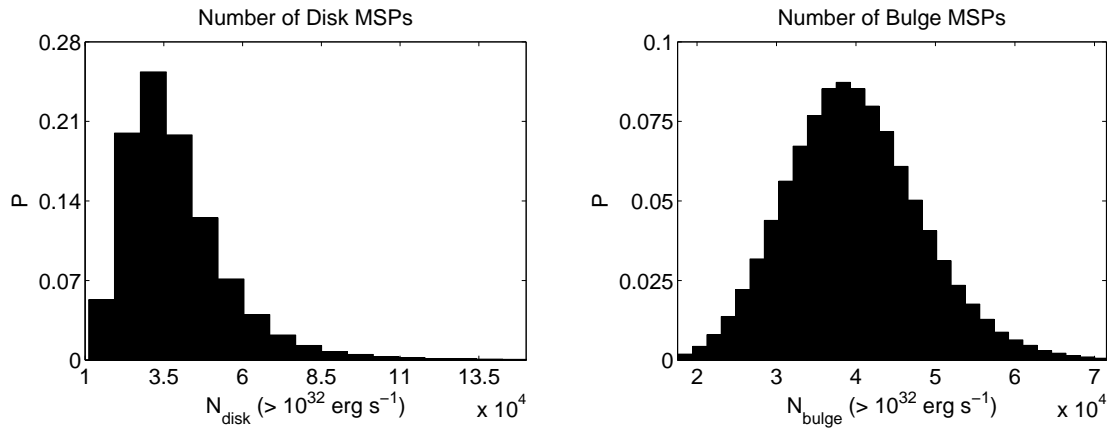


Figure 7. The distribution of the number of MSPs with luminosity greater than $10^{32} \text{ erg} \cdot \text{s}^{-1}$ for the spherical bulge model and lognormal luminosity function.

3.2 X-shaped Bulge

This section presents the results for the spatial model which has an X-shaped bulge. The MCMC simulation results are shown in figure 8. There are, as for the spherically symmetric bulge case, clear correlations between $\log_{10}(L_{\text{med}})$ and σ_L and between the three parameters $\ln(r_{\text{d/b}})$, K_{th} and σ_{th} . Means and errors for each of the model parameters are listed in table 4.

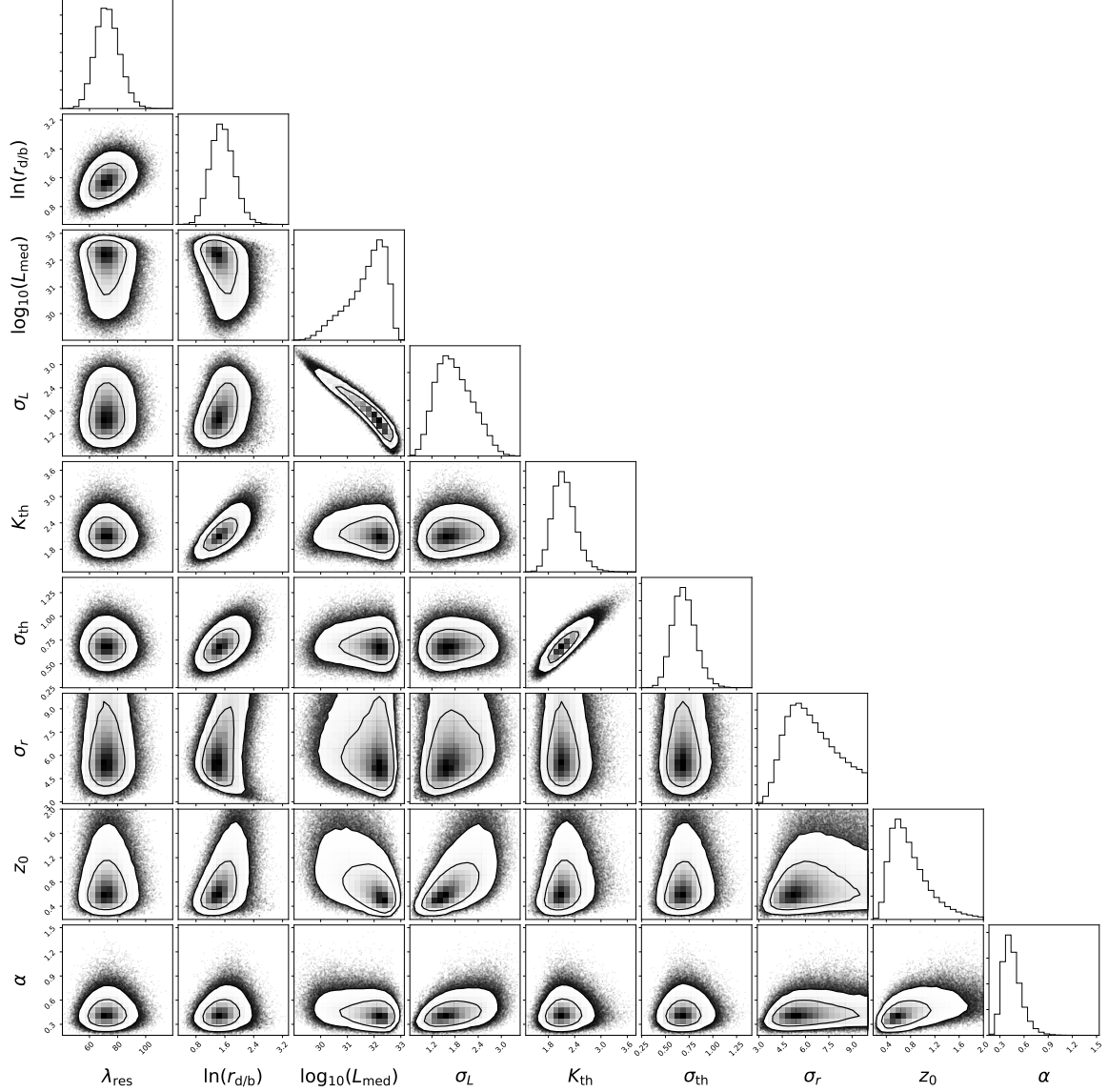


Figure 8. Distribution of points in Markov chains for the lognormal luminosity distribution and X-shaped bulge model. Contours contain 68% and 95% of points. The units of L_{med} and α are ($\text{erg} \cdot \text{s}^{-1}$) and kpc respectively.

The simulated GCE and simulated distributions of resolved MSPs in longitude, latitude, distance and flux are shown in figure 9, with the distribution of the numbers located inside and outside the region of the projected bulge displayed in figure 10.

Parameter	Mean	Error
λ_{res}	73	9
$\ln(r_{\text{d/b}})$	1.5	0.3
$\log_{10}(L_{\text{med}}/(\text{erg} \cdot \text{s}^{-1}))$	31.7	0.7
σ_L	1.8	0.5
K_{th}	2.2	0.3
σ_{th}	0.7	0.1
σ_r/kpc	6	2
z_0/kpc	0.8	0.3
α/kpc	0.5	0.1

Table 4. Mean values and 68% confidence interval errors for lognormal luminosity distribution and X-shaped bulge model parameters.

The probabilities of observing one or more bulge MSPs and the expected number of observations are listed in table 5 with the probability distribution of observing N bulge MSPs displayed in figures 11 and 12. The number of MSPs in the disk with luminosity greater than $10^{32} \text{ erg} \cdot \text{s}^{-1}$ was $(3 \pm 1) \times 10^4$ and the number in the bulge was $(7 \pm 2) \times 10^3$. In figure 13, the distribution of the number of MSPs simulated in the disk and bulge is shown.

Sensitivity Factor	Mean N	$P(N > 0)$
1.0	0.999	0.511
2.0	3.58	0.854
4.0	11.7	0.990

Table 5. Expected number of observed MSPs located in the bulge and probability of observing one or more for lognormal luminosity distribution and X-shaped bulge model.

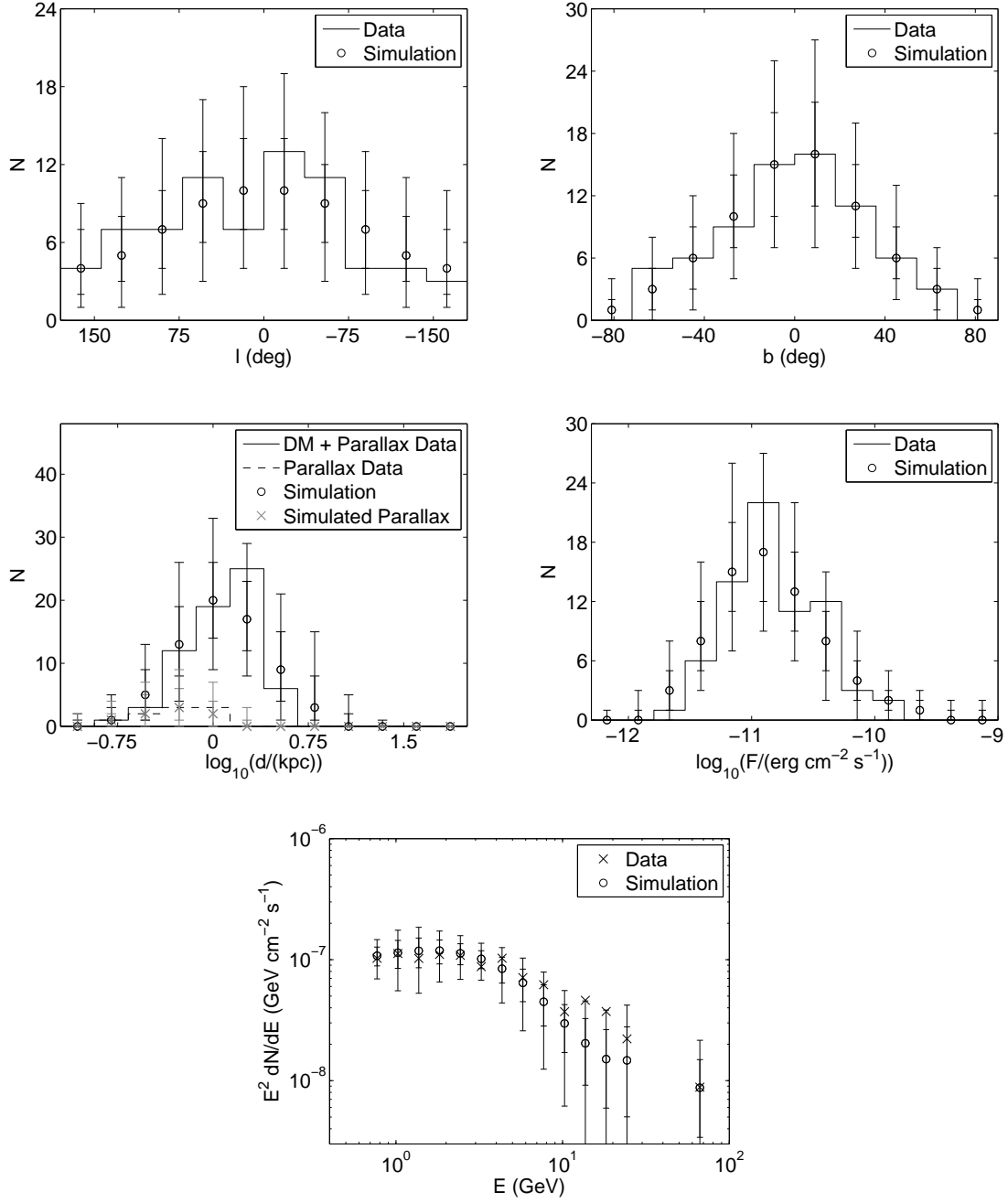


Figure 9. Simulated observed distribution of MSPs in longitude, latitude, distance and flux, and simulated Galactic Center excess for the lognormal luminosity distribution and X-shaped bulge model. In the distance plot, DM means dispersion measure derived distances. The simulated points and error bars are the median, 68% and 95% intervals of the simulated populations in each bin. The error bars on the simulated GCE include the errors on the observed data. Note that the last bin covers the $28 \text{ GeV} \leq E \leq 158 \text{ GeV}$ range.

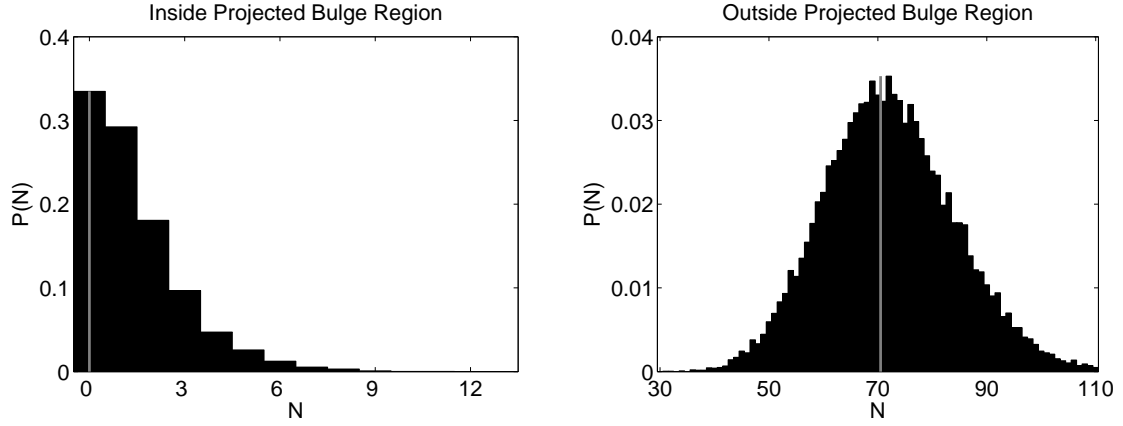


Figure 10. The approximate probability distributions of observing N MSPs inside and outside the projected bulge using the lognormal luminosity distribution and X-shaped bulge model. Here the projected bulge region is the inner $15^\circ \times 15^\circ$ around the GC for which the X-bulge template of ref. [57] is non-zero. The gray lines are the observed number for each case.

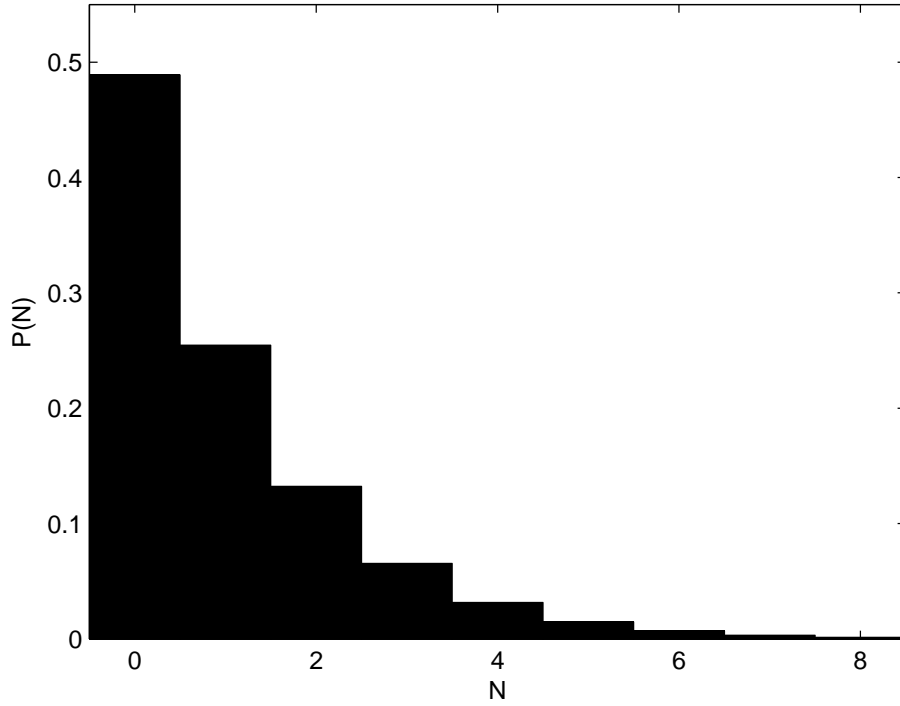


Figure 11. The probability distribution of observing N MSPs from the bulge population based on the lognormal luminosity distribution and X-shaped bulge model.

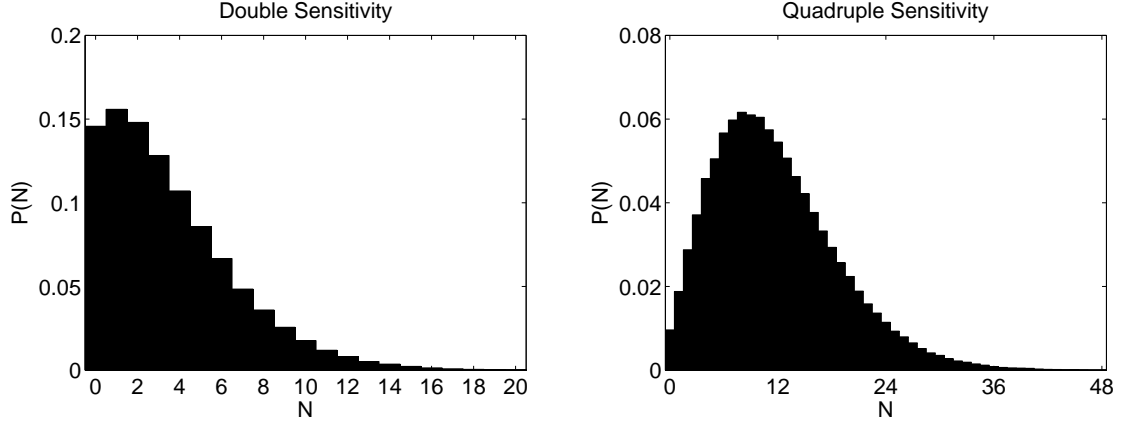


Figure 12. The probability distribution of observing N MSPs from the bulge population based on the lognormal luminosity distribution and X-shaped bulge model with double or quadruple sensitivity.

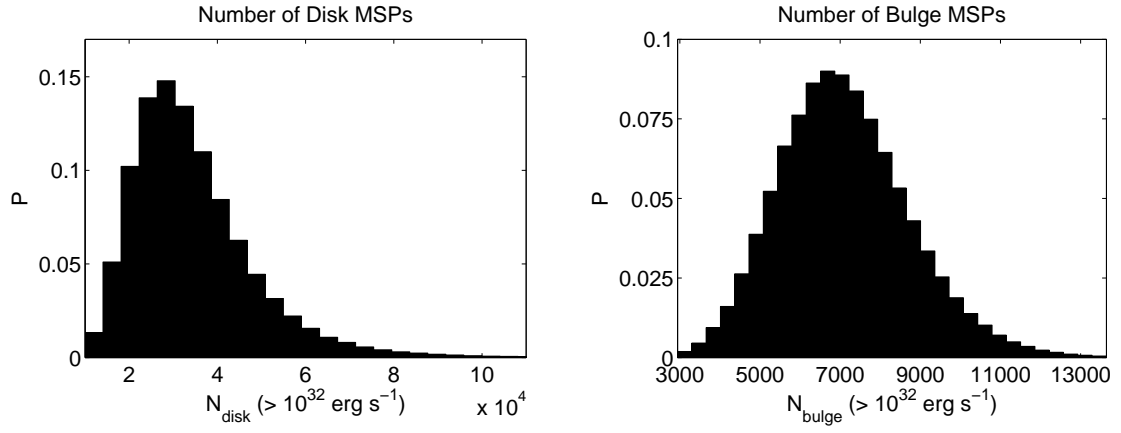


Figure 13. The distribution of the number of MSPs with luminosity greater than $10^{32} \text{ erg} \cdot \text{s}^{-1}$ for the lognormal luminosity function and X-shaped bulge model.

4 Discussion

Figures 3 and 9 show simulated data produced using parameter sets in the Markov chains for the spherical and X-bulge. As can be seen in the top panels, the simulated distributions of resolved MSPs in longitude, latitude and flux are consistent with those observed. All the posterior predicted p-values were in the 0.025 to 0.975 required range corresponding to the 95% error bar, except the 11th point of the last panel of figure 9, which has a predictive p-value of 0.021. The 12th point is very close with a p-value of 0.028. However, these badly fitted points have minimal effect on the parameter fit values as they are high energy GCE points and the parameters are mainly influenced by the lower energy GCE points which have a better signal to noise ratio. The two points may be indications of secondary emission from the bulge MSPS [58].

Although only distances measured using parallax were included as priors on the distance parameters, as can be seen from the left middle panel, the distance distributions of simulated resolved MSPs for both models are similar to that observed, including those distances estimated using the dispersion measure. This indicates the dispersion measure distance may not be biased. The simulated parallax distance distributions are also good fits to the data.

For the spherically symmetric bulge model, the overall goodness of fit p-values, calculated as described at the end of Section 2, were $0.7^{+0.2}_{-0.3}$ for resolved MSPs and $0.14^{+0.13}_{-0.02}$ for the GCE spectrum. For the X-shaped bulge model, these were $0.7^{+0.2}_{-0.3}$ and $0.57^{+0.10}_{-0.05}$ respectively. These results indicate that the model is an acceptable fit to the observed data.

The simulated flux distribution, seen in the middle right hand side panels, requires the uncertain flux threshold to fit the data. When instead of F_{th} being drawn from a lognormal distribution, σ_{th} was removed as a parameter and the threshold was simply $\exp(\mu_{\text{th}}(l, b) + K_{\text{th}})$, the MCMC simulation produces Markov chains with parameters which predict a significantly larger number of resolved low flux MSPs and few higher flux MSPs, resulting in a poor fit to the flux distribution. It is reassuring that our estimated number of disk MSPs in figure 7 and 13 are consistent with the number of disk MSPs from radio observations [59]. But a more detailed investigation is needed to properly compare the radio and gamma-ray results.

Comparing tables 2 and 4 it can be seen that a mildly significant difference between the spherically symmetric and X-shaped bulge models is the ratio $r_{\text{d/b}}$. The number of MSPs in the spherically symmetric bulge is similar to the number of disk MSPs. This is not the case when the X-shaped bulge model is used; here the number of disk MSPs is on average a factor of four larger. It can be seen that this difference is significant at the 3.8σ level when accounting for the uncertainties in the parameter $\ln(r_{\text{d/b}})$ by considering $|\mu_1 - \mu_2|/\sqrt{\sigma_1^2 + \sigma_2^2} = 3.8$ where μ_1 and μ_2 are the means with errors σ_1 and σ_2 for each of the bulge models.

As can be seen from figures 2 and 8 there are correlations between $\ln(r_{\text{d/b}})$, K_{th} and σ_{th} . There are likely two causes for this. The first is that if K_{th} increases, so must σ_{th} ; if it does not, the probability of observing an MSP with flux F_i , $p(F_i > F_{\text{th},i})$, may drop significantly for those MSPs where the measured flux is around the central flux threshold $\exp(\mu_{\text{th}}(l_i, b_i) + K_{\text{th}})$. The other cause of the correlation between the three variables is that if the flux threshold generally increases due to an increase in the parameter K_{th} , the number of MSPs must increase to compensate for the decrease in resolved MSPs. Combined with the fact that bulge MSPs are unlikely to be observed – which means N_{bulge} is largely dependent on the GCE and the luminosity function – the increase occurs in N_{disk} , causing the parameter $r_{\text{d/b}}$ to be higher. The correlation between $\ln(r_{\text{d/b}})$ and σ_{th} is then caused by the other two relationships.

There are also correlations between $\log_{10}(L_{\text{med}})$ and σ_L . This occurs because the observed data could be explained either by a large underlying population of MSPs with a broad distribution of

luminosities and a median lower than those observed or, alternatively, a smaller population of MSPs with a narrow luminosity distribution and median luminosity similar to the observed MSPs. It is likely the luminosity distribution is also, to some extent, constrained by the distribution of resolved MSPs in the sky. For example, a broad luminosity function with a relatively high median would tend to produce distant resolved MSPs that would be clustered in the direction of the GC. This occurs not only because of the bulge model, but also because the peak density of the disk spatial model is there. On the other hand, a narrow luminosity function with a relatively low median would result in the distribution of resolved MSPs being more evenly distributed in the sky (except at low latitudes due to the higher flux threshold). This is a result of the fact that MSPs which pass the flux threshold test would tend to be nearby, and therefore would be found in a volume throughout which the density of MSPs is approximately constant.

The spatial distribution is not particularly well constrained by the data, at the upper limit placed on σ_r the likelihood remains relatively high. However, other work based on simulations and radio data suggests the radial distribution would not be as broad as that at this boundary [51, 53].

The radial extent of the spherically symmetric bulge (r_{bulge}) is determined from the COBE-DIRBE NIR maps to be around 3 kpc [46]. Also, to make our results more easily comparable with ref. [25] we used $r_{\text{bulge}} = 3.1$ kpc. We checked the sensitivity of the results to the radial extent of the spherically symmetric bulge by constructing a Markov chain for each of the cases where the bulge was larger or smaller in radius by 1 kpc. The only clear change in the parameter distribution was small shifts in $\ln(r_{\text{d/b}})$, this likely occurred as when the bulge is spread out, the bulge MSP density will drop and so decrease the GCE unless the number of bulge MSPs is increased. The other change was in the expected number of resolved bulge MSPs, rising to 2.0 for a 4.1 kpc bulge radius and decreasing to 1.0 for the 2.1 kpc radius. As seen in Table 3, the expectation value was 1.4 for the 3.1 kpc bulge case.

Our parameter fits for K_{th} and σ_{th} can be used to visualize the stochastic selection function we are using based on eq. (2.5). We illustrate a sample from this distribution in figure 14. Note that this image is only illustrative as if a pixel contains more than one MSP then each MSP in that pixel will be a separate draw from the distribution. This figure may be qualitatively compared with figure 16 of ref. [48] which has also had some clipping applied. Although, note that each step in the Markov chain will generate a new sample of K_{th} and σ_{th} and so a new threshold map.

Ref. [25] used the observed MSPs to attempt to find parameters for the lognormal luminosity function by using the product of three binned likelihoods one for longitude, one for latitude, and the other for flux [60]. In each bin the expected number of observations λ_i was found by taking a large number of random samples from the model, binning them, and normalizing so that $\sum_{i=1}^N \lambda_i = 66$, where 66 was the number of MSPs used in their fit. Their likelihood for each distribution was:

$$\mathcal{L} = \prod_i \frac{\lambda_i^{n_i} \exp(-\lambda_i)}{n_i!} \quad (4.1)$$

where n_i was the number of observed MSPs in bin i . The results are compared to the results of this work for both the spherically symmetric and X-shaped bulge models in figures 15 and 16. While there is some agreement, the difference could be explained in part by the use of the parallax measured distances which were only used to estimate a lower bound on σ_L in ref. [25]. The other significant difference between that study and this work is the separable form of likelihood they used. As seen from eq. (2.10), the actual likelihood will not be separable in this way. We included, in addition, the bulge model as part of the likelihood, not only to find parameters fitting the GCE, but also because some luminosity distributions could result in many observed bulge MSPs. This could reduce the likelihood for luminosity functions that tend to generate high luminosity MSPs with greater probability.

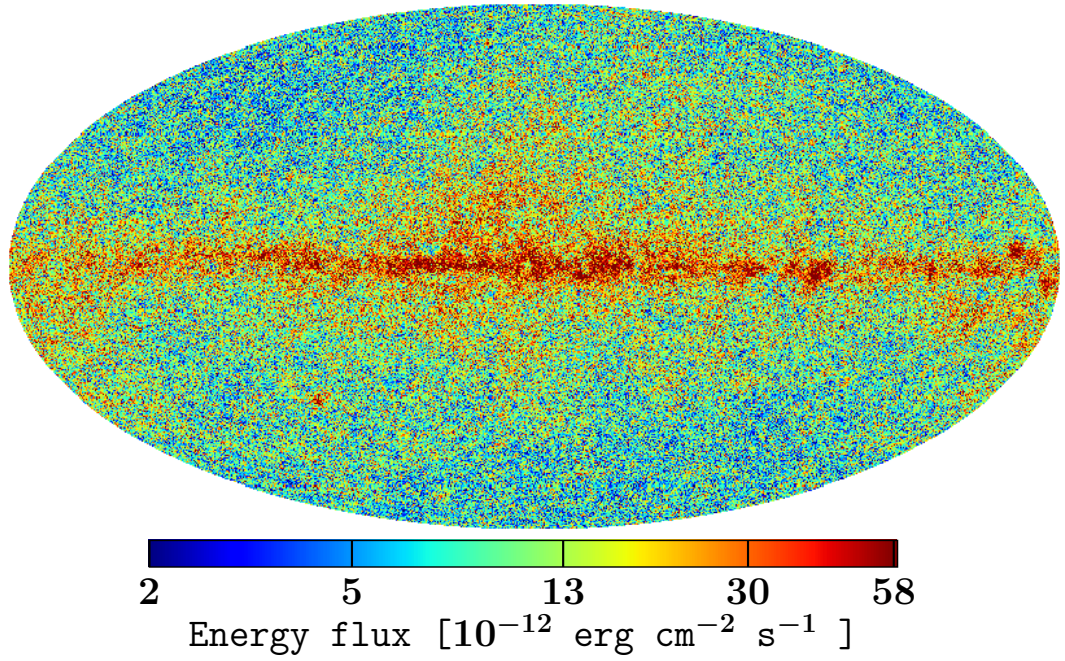


Figure 14. Hammer-Aitoff projection of a sample threshold map, for flux above 100 MeV, from eq. (2.5) using our mean posterior fit values from table 2. For display purposes we have clipped the upper and lower 2.5% pixels.

Figures 15 and 16 also show the luminosity function parameter distribution which results when the contribution of resolved bulge MSPs is removed. Based on the fitted flux threshold, we found a mean of 12.8 resolved spherical bulge MSPs, and the probability of observing one or more was 0.959. The probability distribution is shown in figure 17. It is also suggested in ref. [25] that a further restriction can be placed on the luminosity function parameters by considering MSPs located in globular clusters. These were not taken into account here as it is unlikely they would have the same luminosity distribution as the disk population.

It is concluded in ref. [25] that many MSPs located in the bulge should have already been observed if the luminosity distribution were the same for disk and bulge MSPs. While the probability of observing bulge MSPs varies depending on the model used as can be seen from tables 3 and 5, we find that there is a significant probability that no bulge MSPs would have been resolved based on the fitted threshold and luminosity function parameters. Although six of the observed MSPs are inside the solid angle of the projected spherically symmetric bulge, the distances estimated using dispersion measures indeed indicate that none are actually located inside this bulge. No MSPs were observed in the region of the projected X-shaped bulge. With four times the current sensitivity to point sources it is likely that many bulge MSPs could be resolved. Double the current sensitivity could result in a few observations.

As the work for this article was completed, a new article on a pulsar explanation of the GCE by the Fermi team was made available [15]. In this new work, a power law was used to model the luminosity distribution of both young pulsars and MSPs combined. This was of the form $dN/dL \propto L^{-\beta}$ for L between $L_{\min} = 10^{31} \text{ erg} \cdot \text{s}^{-1}$ and $L_{\max} = 10^{36} \text{ erg} \cdot \text{s}^{-1}$ and zero outside that range. They found the luminosity distribution of nearby pulsars can be modeled by $\beta = 1.2$. To determine the number of disk and bulge pulsars, they took as pulsar candidates all detected point sources in a 40° by

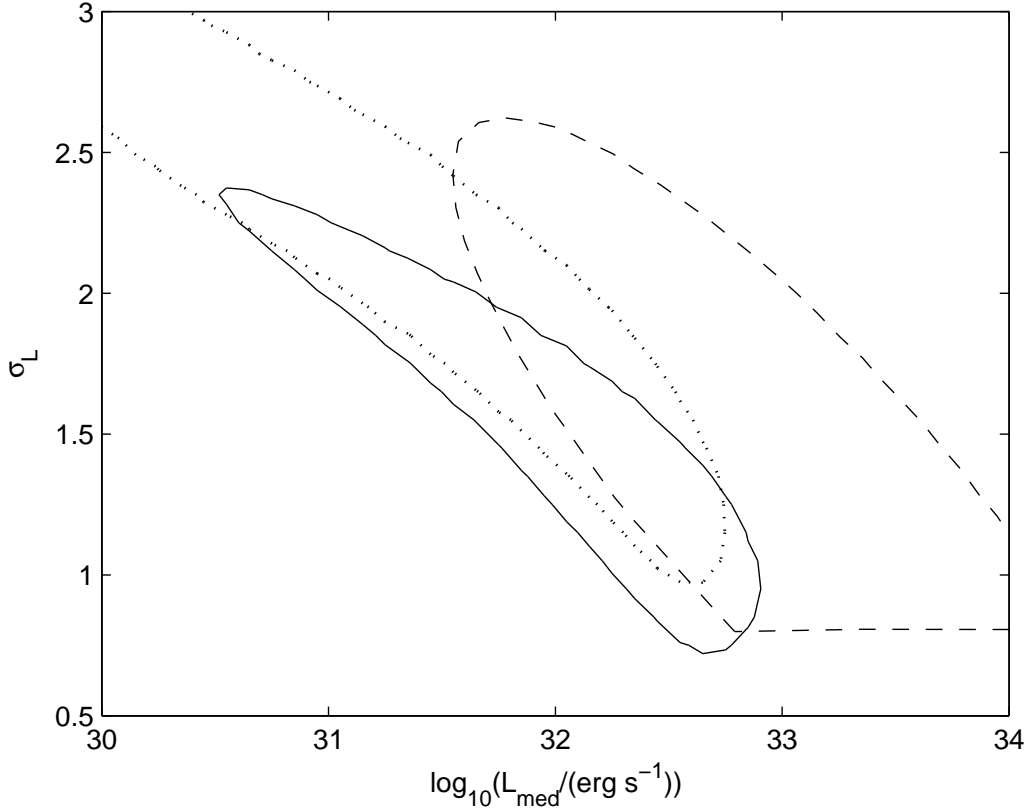


Figure 15. Contour plot of luminosity function parameter distribution showing the 95% contour for the log-normal luminosity distribution and spherical bulge model. The dashed line is the 2σ contour from ref. [25]. The dotted line is the 95% contour for the luminosity function distribution assuming the spherical bulge does not contribute to resolved MSPs.

40° area around the GC which had significantly curved spectra and when fitted, with an exponential cutoff spectrum, had a spectral slope less than 2 and an energy cutoff less than 10 GeV. To compare our resolved MSP constraints to their model, we fitted a disk only power law model with the poorly constrained L_{\min} fixed to 10^{31} erg/s and L_{\max} and β left as free parameters. Marginalizing over the other free parameters, in the same way as we did for the lognormal case, we got the constraints in figure 18. Using the GCE of ref. [12], we found the selection function of figure 18 had a mean number of resolved bulge MSPs which was 0.354 and the probability of resolving one or more was 0.177. But this does not imply the number of pulsar candidates based on the point source spectrum will be this low as ref. [15] did not require the gamma-ray pulsations to be detected. As can be seen, for the resolved MSPs, a lower value of L_{\max} than ref. [15] used is needed for $\beta = 1.2$. Although, as they combined the MSPs and young pulsars, our result is not straight forwardly applicable to their case.

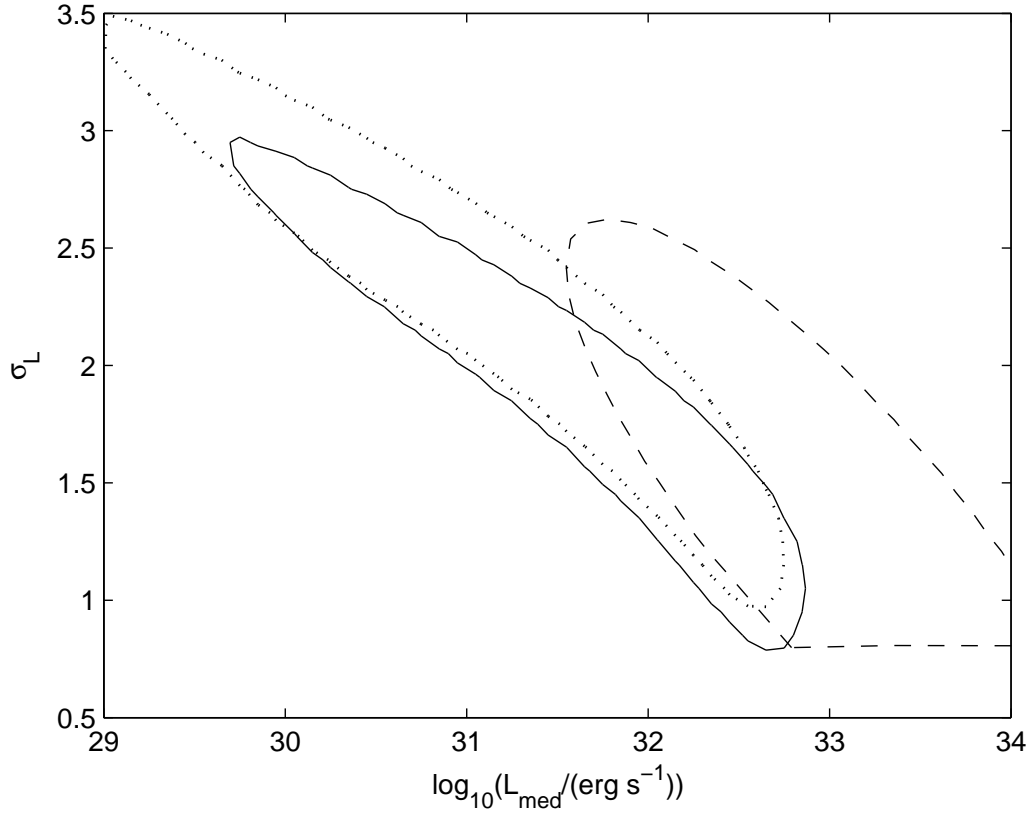


Figure 16. Contour plot of luminosity function parameter distribution showing the 95% contour for the log-normal luminosity distribution and X-shaped bulge model. The dashed line is the 2σ contour from ref. [25]. The dotted line is the 95% contour for the luminosity function distribution assuming the spherical bulge does not contribute to resolved MSPs.

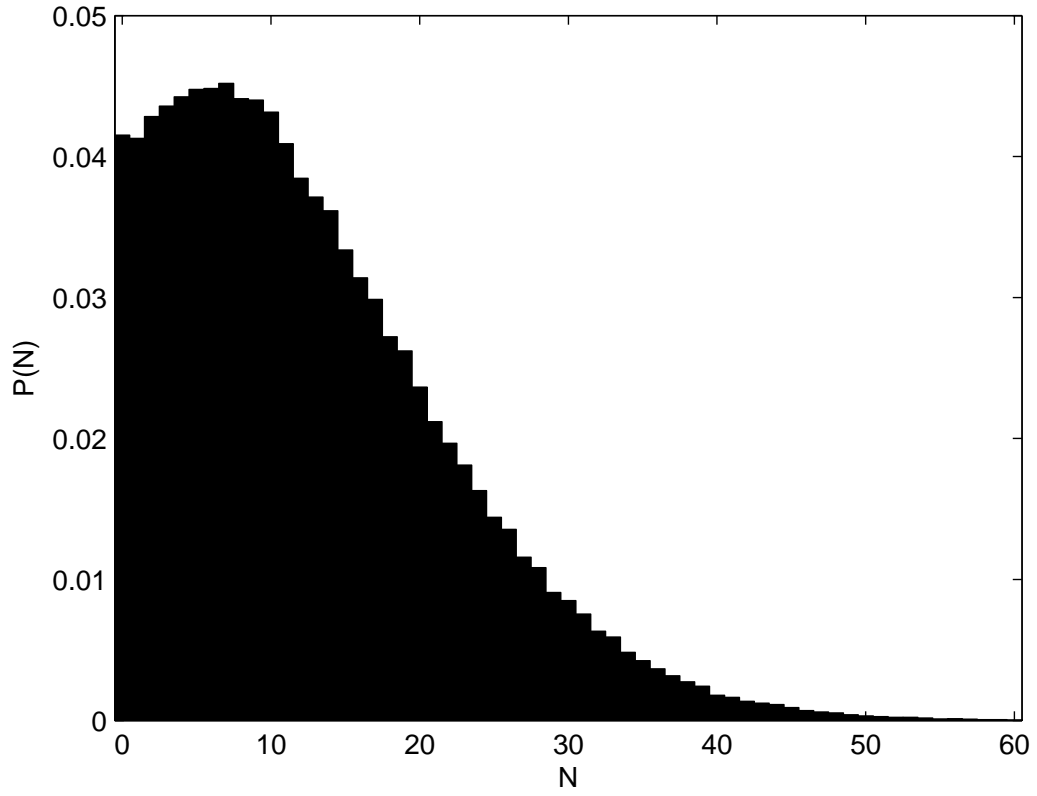


Figure 17. The probability distribution of observing N MSPs from the spherical bulge population based on a lognormal luminosity function fitted assuming only MSPs from the disk model can be observed.

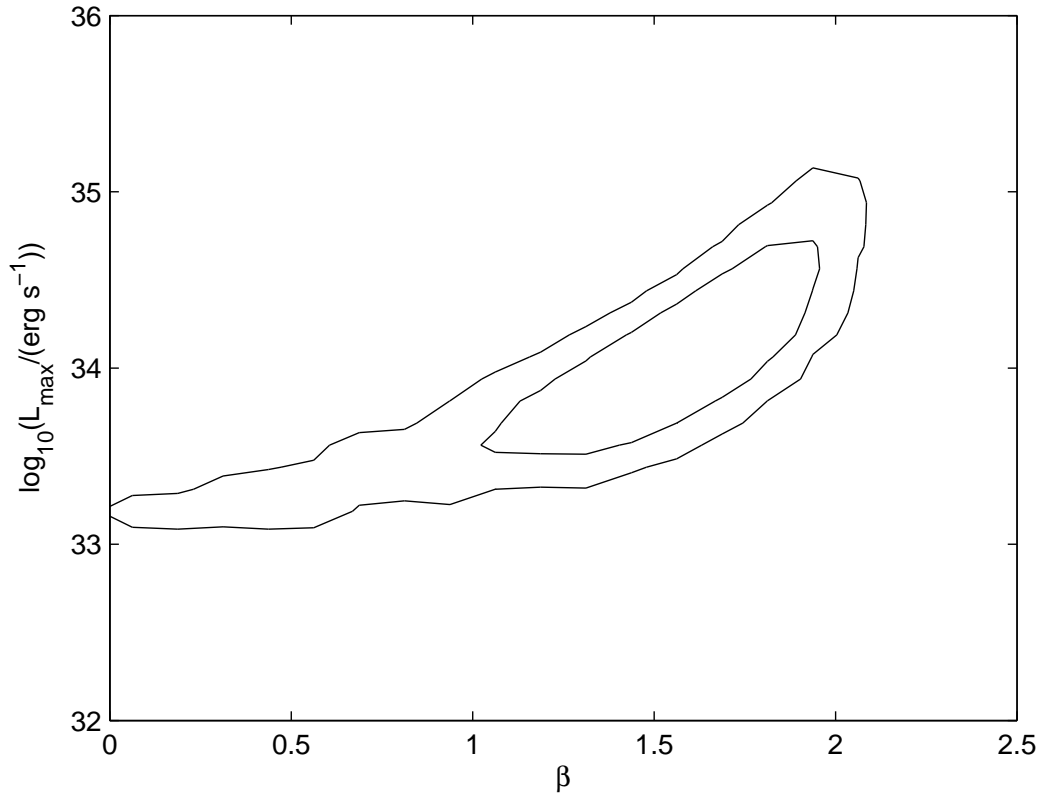


Figure 18. Marginalized confidence intervals (68% and 95%) of a power law luminosity function, $dN/dL \propto L^{-\beta}$, with a maximum luminosity, L_{\max} . These constraints are for a disk only model of the resolved MSPs.

5 Conclusions

An MCMC algorithm was used to constrain parameters for a set of models of the Milky Way MSP population, with the luminosity distribution being of particular interest. This search over the parameter space was performed using the GCE data, the locations of observed MSPs in the sky, their fluxes, and their distances where parallax distance measurements were available.

To confirm that the models could plausibly explain the observations, the Markov chains of parameters produced by the MCMC simulation were then used to produce simulated data. The simulated distributions of resolved MSPs were a good fit to the observed data, as were the simulations of the GCE.

Although it seems unlikely that the disk and bulge MSPs would have the same luminosity function, our results show that the current data are not precise enough to reveal any differences between the two (if they exist). This is mainly because the bulge MSP population is relatively unconstrained by our analysis which is only sensitive to the luminosity of the entire population via the product $\bar{L}N_{\text{bulge}}$ where \bar{L} is the average luminosity. While the constraint that not too many bright, bulge MSPs be predicted does require that the luminosity function not be too skewed too much towards high luminosities, this turns out not to be a very tight constraint given the current point source sensitivity of observations towards the inner Galaxy. As seen from tables 3 and 5 an improvement in the gamma-ray point source detection sensitivity by a factor of around two may allow a number of MSPs from the bulge population to be resolved and hence help test the MSP proposal for the GCE.

It was claimed by ref. [25] that if the GCE were produced by MSPs, many of them would already have been resolved. Here, it has been shown that this is in fact not the case. The main cause of this disagreement is likely due to ref. [25] not including the possibility of resolved bulge MSPs when they evaluated their best fit luminosity function parameters.

As the current article was being completed, ref. [15] presented an analysis based on new bulge pulsar candidates. But, these candidates have not been resolved in the sense of the current 3FGL resolved MSPs in that they do not yet have evidence of gamma-ray pulsations and have not been shown to be coincident with a radio pulsar. In future work we plan to include the 3FGL resolved young pulsars and the new pulsar candidates found in ref. [15] which will need separate selection functions in addition to the one we are currently using in eq. (2.5). We will then use the new luminosity function parameters to update forecasts for future observations, at radio wavelengths, of the bulge pulsars [61].

Acknowledgments

We thank David Smith for providing the numerical values for figure 16 of ref. [48] and also for helpful correspondence. We gratefully acknowledge useful correspondence and conversation with Lilia Ferrario, Dan Hooper, Ivo Seitzzahl, Ashley Ruiters, Simone Scaringi, and Qiang Yuan.

A Supplementary Material

A.1 Computational Methods

To sample a random point from the disk spatial model of eq. (2.2), $|z|$ is drawn from an exponential distribution with scale parameter z_0 , then z is assigned either $|z|$ or $-|z|$ each with probability 0.5. A value for θ is then drawn from a uniform distribution on the interval $[0, 2\pi)$. Finally, r_{cyl} is randomly drawn from the following probability distribution function:

$$f(r) = \frac{1}{\sigma_r^2} \exp(-r_{\text{cyl}}^2/2\sigma_r^2) r_{\text{cyl}} \quad (\text{A.1})$$

The factor of r_{cyl} is related to the volume element $dV = r_{\text{cyl}} dr_{\text{cyl}} dz d\theta$.

Before the posterior distribution can be found it is necessary to find the number of MSPs in the disk and bulge implied by the parameters. Let p_{disk} and p_{bulge} be the probability of an MSP being observed in the disk and bulge respectively, then N_{disk} of eq. (2.3) and N_{bulge} of eq. (2.2) can be found using the following two equations:

$$\begin{aligned}\lambda_{\text{res}} &= p_{\text{disk}} N_{\text{disk}} + p_{\text{bulge}} N_{\text{bulge}} \\ r_{\text{d/b}} &= N_{\text{disk}} / N_{\text{bulge}}\end{aligned}\tag{A.2}$$

Solving for N_{disk} and N_{bulge} gives:

$$\begin{aligned}N_{\text{disk}} &= \frac{\lambda_{\text{res}}}{p_{\text{disk}} + p_{\text{bulge}} / r_{\text{d/b}}} \\ N_{\text{bulge}} &= \frac{\lambda_{\text{res}}}{p_{\text{disk}} r_{\text{d/b}} + p_{\text{bulge}}}\end{aligned}\tag{A.3}$$

It is not practical to find p_{disk} and p_{bulge} exactly as this would require a multidimensional integral for every iteration of the MCMC algorithm. A simplistic way to approximate p_{disk} or p_{bulge} would be to draw a large number of simulated MSPs from the corresponding model (disk or bulge) and use the fraction that are resolved. However, this method has a significant disadvantage: the number of MSPs that it would be necessary to simulate to ensure the result is reasonably accurate could potentially be extremely large. This is because the number of simulated MSPs that are resolved is Poisson distributed, therefore for a relative error of on the order of 1% we may wish to continue drawing from the disk model until we have several thousand resolved (usually $p_{\text{bulge}} \ll p_{\text{disk}}$ and $r_{\text{d/b}} \sim 1$ so accuracy is less important for the bulge), but for luminosity functions which produce few highly luminous MSPs this could mean millions of draws from the model.

There is a simple improvement that can be made by recognizing that position in l , b and d allows a luminosity threshold L_{th} to be found. Before running the MCMC algorithm for each Markov chain, distributions of points were generated according to the bulge and disk spatial models and the position of each point was converted to l , b and d , in addition, for each point, a random number u was drawn from the unit normal distribution to allow us to account for the uncertain flux threshold. Using eq. (2.4) and the fact that the logarithm of the flux threshold is normally distributed with scale parameter σ_{th} , the luminosity threshold for point i is:

$$L_{\text{th},i} = 4\pi d_i^2 \exp(\mu_{\text{th}}(l_i, b_i) + K_{\text{th}} + \sigma_{\text{th}} u_i)\tag{A.4}$$

For any proposed set of parameters we can use importance sampling [62] to evaluate the probability of a single random MSP being observed:

$$p \approx \frac{1}{N} \sum_{i=1}^N w_i p(L > L_{\text{th},i})\tag{A.5}$$

where N is the total number of points, $p(L > L_{\text{th},i})$ is the probability that a randomly generated luminosity is greater than the threshold and p represents either p_{disk} or p_{bulge} . As the spatial parameters are allowed to vary, the spatial distribution of MSPs we are interested in is not the same as that which the points were sampled from. For point i , w_i is the spatial density of MSPs given by the parameters divided by the density of points. Because the same spatial distribution of points and

distribution of u_i is used for each iteration of the algorithm, it can be guaranteed that a particular set of parameters will always give the same result for N_{disk} and N_{bulge} . A further improvement that was made involved generating nearer points with higher probability. This ensures a larger proportion of points have relatively low $L_{\text{th},i}$. Without this, if the luminosity function parameters give a distribution heavily weighted towards lower luminosities, p might effectively depend on a relatively small number of points. Not only could this result in larger errors, but if this issue is resolved by simply generating more points, it also means a large amount of time is spent evaluating $p(L > L_{\text{th},i})$ which have a negligible contribution.

A.2 Resolved MSP Data

Name	l (deg)	b (deg)	Flux (10^{-11} erg cm $^{-2}$ s $^{-1}$)	Γ (or ω)	E_{cut} (GeV)	β	E_0 (GeV)	d (kpc)
J0023+0923	111.5	-52.9	0.73 \pm 0.08	1.0 \pm 0.3	1.0 \pm 0.2	-	0.90	0.7 \pm 0.1
J0030+0451	113.1	-57.6	6.1 \pm 0.2	1.28 \pm 0.05	2.1 \pm 0.2	-	0.76	0.28 $^{+0.1}_{-0.06}$ (P)
J0034-0534	111.5	-68.1	1.8 \pm 0.1	1.7 \pm 0.1	2.9 \pm 0.6	-	0.70	0.5 \pm 0.1
J0101-6422	301.2	-52.7	1.25 \pm 0.09	1.5 \pm 0.1	2.9 \pm 0.6	-	0.90	0.55 $^{+0.09}_{-0.08}$
J0102+4839	124.9	-14.2	1.7 \pm 0.1	1.8 \pm 0.1	6 \pm 2	-	1.2	2.3 $^{+0.5}_{-0.4}$
J0218+4232	139.5	-17.5	4.8 \pm 0.2	1.94 \pm 0.06	4.7 \pm 0.8	-	0.74	2.7 $^{+1.1}_{-0.7}$
J0251+26	153.9	-29.5	0.7 \pm 0.1	2.3 \pm 0.1	-	-	1.1	0.8 $^{+0.2}_{-0.1}$
J0307+7443	131.7	14.2	1.46 \pm 0.08	0.5	1.24 \pm 0.07	-	1.9	-
J0340+4130	153.8	-11.0	2.2 \pm 0.1	1.3 \pm 0.1	3.8 \pm 0.7	-	1.4	1.7 \pm 0.3
J0437-4715	253.4	-42.0	1.79 \pm 0.09	1.3 \pm 0.1	1.0 \pm 0.2	-	0.59	0.156 \pm 0.001 (P)
J0533+6759	144.8	18.2	0.96 \pm 0.09	1.6 \pm 0.2	6 \pm 2	-	1.4	2.4 $^{+0.9}_{-0.6}$
J0605+3757	174.2	8.0	0.7 \pm 0.1	0.7 \pm 0.4	1.5 \pm 0.4	-	1.5	0.7 \pm 0.1
J0610-2100	227.7	-18.2	1.1 \pm 0.1	2.34 \pm 0.07	-	-	0.85	-
J0613-0200	210.4	-9.3	3.4 \pm 0.2	1.4 \pm 0.1	2.9 \pm 0.4	-	1.1	0.9 $^{+0.4}_{-0.2}$ (P)
J0614-3329	240.5	-21.8	11.1 \pm 0.2	1.36 \pm 0.03	4.7 \pm 0.3	-	0.88	1.9 \pm 0.4
J0621+2514	187.1	5.1	1.1 \pm 0.1	2.17 \pm 0.09	-	-	1.7	2.3 $^{+0.5}_{-0.4}$
J0751+1807	202.8	21.1	1.3 \pm 0.1	1.3 \pm 0.2	3.0 \pm 0.6	-	1.2	0.4 $^{+0.2}_{-0.1}$ (P)
J0931-1902	251.0	23.0	0.30 \pm 0.09	1.8 \pm 0.2	-	-	3.4	1.9 $^{+0.5}_{-0.4}$
J0955-61	283.7	-5.7	0.8 \pm 0.1	2.3 \pm 0.1	-	-	1.2	4.0 $^{+0.9}_{-0.8}$
J1024-0719	251.7	40.5	0.36 \pm 0.05	0.5	1.4 \pm 0.2	-	2.1	0.39 \pm 0.04
J1124-3653	284.1	22.8	1.3 \pm 0.1	1.3 \pm 0.2	3.1 \pm 0.7	-	1.4	1.7 \pm 0.4
J1125-5825	291.8	2.6	1.5 \pm 0.3	2.4 \pm 0.1	-	-	1.9	2.6 \pm 0.4
J1125-6014	292.5	0.9	1.2 \pm 0.3	2.4 \pm 0.1	-	-	2.1	1.5 \pm 0.2
J1137+7528	129.1	40.8	0.23 \pm 0.06	2.3 \pm 0.2	-	-	1.5	-
J1142+0119	267.6	59.4	0.62 \pm 0.08	1.2 \pm 0.3	5 \pm 2	-	1.8	0.9 \pm 0.2
J1207-5050	295.9	11.4	0.8 \pm 0.1	2.1 \pm 0.1	-	-	1.5	1.5 \pm 0.2
J1227-4853	299.0	13.8	4.1 \pm 0.2	2.23 \pm 0.05	-	0.11 \pm 0.03	0.44	1.4 \pm 0.2

Name	l (deg)	b (deg)	Flux (10^{-11} erg cm $^{-2}$ s $^{-1}$)	Γ (or ω)	E_{cut} (GeV)	β	E_0 (GeV)	d (kpc)
J1231-1411	295.5	48.4	10.3 ± 0.2	1.18 ± 0.04	2.6 ± 0.2	-	0.92	0.44 ± 0.05
J1301+0833	310.8	71.3	1.1 ± 0.1	2.4 ± 0.1	-	-	0.77	0.7 ± 0.1
J1302-3258	305.6	29.8	1.1 ± 0.1	1.1 ± 0.2	2.7 ± 0.7	-	1.4	1.0 ± 0.2
J1311-3430	307.7	28.2	6.5 ± 0.2	1.91 ± 0.05	5.1 ± 0.8	-	0.66	1.4 ± 0.3
J1312+0051	314.8	63.2	1.6 ± 0.1	1.5 ± 0.1	2.8 ± 0.6	-	0.84	$0.8^{+0.2}_{-0.1}$
J1400-1438	326.9	45.0	0.9 ± 0.1	2.30 ± 0.08	-	-	0.95	0.48 ± 0.03
J1446-4701	322.5	11.4	1.3 ± 0.1	2.30 ± 0.08	-	-	1.0	1.5 ± 0.2
J1514-4946	325.2	6.8	4.3 ± 0.2	1.43 ± 0.09	5.0 ± 0.7	-	1.5	0.9 ± 0.1
J1536-4948	328.2	4.8	8.7 ± 0.3	1.87 ± 0.03	-	0.17 ± 0.02	1.0	1.8 ± 0.1
J1543-5149	327.9	2.7	2.2 ± 0.3	2.5 ± 0.1	-	-	0.83	2.4 ± 0.2
J1544+4937	79.2	50.2	0.36 ± 0.06	2.3 ± 0.1	-	-	1.1	$1.2^{+0.4}_{-0.3}$
J1600-3053	344.1	16.5	0.6 ± 0.1	1.0 ± 0.5	3 ± 2	-	2.6	1.6 ± 0.3
J1614-2230	352.6	20.2	2.3 ± 0.1	0.8 ± 0.2	1.8 ± 0.3	-	1.4	0.65 ± 0.05 (P)
J1628-3205	347.4	11.5	1.2 ± 0.1	2.3 ± 0.1	-	0.4 ± 0.1	1.0	1.3 ± 0.2
J1630+3734	60.2	43.3	0.7 ± 0.1	1.0 ± 0.4	2.0 ± 0.6	-	1.6	0.9 ± 0.1
J1658-5324	334.9	-6.6	2.0 ± 0.2	1.4 ± 0.2	1.4 ± 0.3	-	1.0	0.9 ± 0.1
J1713+0747	28.8	25.2	0.9 ± 0.1	1.4 ± 0.3	3 ± 1	-	1.4	$1.05^{+0.06}_{-0.05}$
J1732-5049	340.0	-9.4	0.9 ± 0.1	2.4 ± 0.1	-	-	0.96	1.4 ± 0.2
J1741+1351	37.9	21.6	0.6 ± 0.1	2.2 ± 0.1	-	-	1.3	$1.08^{+0.04}_{-0.05}$ (P)
J1744-1134	14.8	9.2	3.9 ± 0.2	1.4 ± 0.1	1.5 ± 0.2	-	0.75	0.42 ± 0.02 (P)
J1745+1017	34.9	19.3	1.1 ± 0.1	1.5 ± 0.3	4 ± 1	-	1.5	$1.3^{+0.2}_{-0.1}$
J1747-4036	350.2	-6.4	1.6 ± 0.2	2.3 ± 0.1	-	-	1.2	3.4 ± 0.8
J1805+06	33.4	13.0	0.5 ± 0.1	1.7 ± 0.3	-	0.6 ± 0.2	1.9	$2.5^{+0.5}_{-0.4}$
J1810+1744	44.6	16.8	2.2 ± 0.1	1.8 ± 0.1	2.9 ± 0.7	-	0.66	$2.0^{+0.3}_{-0.2}$
J1816+4510	72.9	24.8	1.21 ± 0.09	1.7 ± 0.1	5 ± 1	-	0.91	$2.4^{+0.7}_{-0.4}$
J1843-1113	22.0	-3.4	2.0 ± 0.3	2.7 ± 0.1	-	-	0.50	1.7 ± 0.2
J1858-2216	13.6	-11.4	0.8 ± 0.1	0.7 ± 0.4	1.8 ± 0.6	-	1.6	0.9 ± 0.1
J1902-5105	345.6	-22.4	2.1 ± 0.1	1.8 ± 0.1	3.5 ± 0.9	-	0.62	1.2 ± 0.2
J1903-7051	324.4	-26.5	1.2 ± 0.1	2.32 ± 0.07	-	-	0.91	0.8 ± 0.1

Name	l (deg)	b (deg)	Flux (10^{-11} erg cm $^{-2}$ s $^{-1}$)	Γ (or ω)	E_{cut} (GeV)	β	E_0 (GeV)	d (kpc)
J1959+2048	59.2	-4.7	1.8 ± 0.2	1.3 ± 0.2	1.4 ± 0.3	-	0.80	$2.5^{+0.2}_{-0.5}$
J2017+0603	48.6	-16.0	3.5 ± 0.2	1.1 ± 0.1	3.7 ± 0.5	-	1.7	1.6 ± 0.2
J2042+0246	49.0	-23.0	0.36 ± 0.06	2.3 ± 0.3	-	1	1.2	-
J2043+1711	61.9	-15.3	3.0 ± 0.1	1.58 ± 0.08	4.5 ± 0.8	-	0.96	$1.8^{+0.1}_{-0.3}$
J2047+1053	57.1	-19.6	0.36 ± 0.06	0.5	1.7 ± 0.3	-	2.6	2.1 ± 0.3
J2051-0827	39.2	-30.5	0.32 ± 0.05	0.5	1.6 ± 0.3	-	2.4	$1.0^{+0.2}_{-0.1}$
J2124-3358	10.9	-45.4	3.9 ± 0.1	0.9 ± 0.1	1.9 ± 0.2	-	1.1	$0.30^{+0.07}_{-0.05}$ (P)
J2129-0429	48.9	-36.9	1.0 ± 0.1	2.22 ± 0.07	-	-	1.0	0.9 ± 0.1
J2214+3000	86.9	-21.7	3.3 ± 0.1	1.20 ± 0.08	2.4 ± 0.3	-	0.94	1.5 ± 0.2
J2215+5135	99.9	-4.2	1.4 ± 0.1	1.4 ± 0.2	3.5 ± 0.8	-	1.3	$3.0^{+0.3}_{-0.4}$
J2234+0944	76.3	-40.4	0.8 ± 0.1	1.3 ± 0.3	2.1 ± 0.7	-	1.1	-
J2241-5236	337.4	-54.9	3.1 ± 0.1	1.25 ± 0.08	2.8 ± 0.4	-	0.94	0.51 ± 0.08
J2256-1024	59.2	-58.2	0.77 ± 0.08	1.2 ± 0.2	2.3 ± 0.6	-	1.2	0.6 ± 0.1
J2302+4442	103.4	-14.0	3.8 ± 0.1	1.19 ± 0.08	3.0 ± 0.3	-	1.1	$1.2^{+0.1}_{-0.2}$
J2339-0533	81.3	-62.5	3.0 ± 0.1	1.51 ± 0.08	5.1 ± 0.9	-	0.96	-

Table 6: List of observed millisecond pulsars. For the spectral parameters, MSPs with neither the E_{cut} or β columns filled have been fitted with a simple power law spectrum, those with E_{cut} filled have been fitted with an exponentially cutoff power law, and those with the β column filled have been fitted with a log parabolic spectrum. Data from 3FGL catalog [63] except distance measurements. A (P) in the distance column indicates the distance is that reported in ref. [48] and was found using the parallax method. Other distances were derived from the dispersion measure reported in the ATNF pulsar catalog [44] using the NE2001 model [64].

References

- [1] L. Goodenough and D. Hooper, *Possible Evidence For Dark Matter Annihilation In The Inner Milky Way From The Fermi Gamma Ray Space Telescope*, *ArXiv e-prints (arXiv:0910.2998)* (Oct., 2009) , [[0910.2998](#)].
- [2] D. Hooper and T. Linden, *On The Origin Of The Gamma Rays From The Galactic Center*, *Phys. Rev. D* **84** (2011) 123005, [[1110.0006](#)].
- [3] K. N. Abazajian and M. Kaplinghat, *Detection of a Gamma-Ray Source in the Galactic Center Consistent with Extended Emission from Dark Matter Annihilation and Concentrated Astrophysical Emission*, *Phys. Rev. D* **86** (2012) 083511, [[1207.6047](#)].
- [4] C. Gordon and O. Macias, *Dark Matter and Pulsar Model Constraints from Galactic Center Fermi-LAT Gamma Ray Observations*, *Phys. Rev. D* **88** (2013) 083521, [[1306.5725](#)].
- [5] O. Macias and C. Gordon, *Contribution of cosmic rays interacting with molecular clouds to the Galactic Center gamma-ray excess*, *Phys. Rev. D* **89** (2014) 063515, [[1312.6671](#)].
- [6] K. N. Abazajian, N. Canac, S. Horiuchi and M. Kaplinghat, *Astrophysical and Dark Matter Interpretations of Extended Gamma-Ray Emission from the Galactic Center*, *Phys. Rev. D* **90** (2014) 023526, [[1402.4090](#)].
- [7] T. Daylan, D. P. Finkbeiner, D. Hooper, T. Linden, S. K. N. Portillo, N. L. Rodd et al., *The characterization of the gamma-ray signal from the central Milky Way: A case for annihilating dark matter*, *Phys. Dark Univ.* **12** (2016) 1–23, [[1402.6703](#)].
- [8] B. Zhou, Y.-F. Liang, X. Huang, X. Li, Y.-Z. Fan, L. Feng et al., *GeV excess in the Milky Way: The role of diffuse galactic gamma-ray emission templates*, *Phys. Rev.* **91** (June, 2015) 123010, [[1406.6948](#)].
- [9] F. Calore, I. Cholis and C. Weniger, *Background model systematics for the Fermi GeV excess*, *J. Cosm. & Astropart. Phys.* **3** (Mar., 2015) 38, [[1409.0042](#)].
- [10] FERMI-LAT collaboration, M. Ajello et al., *Fermi-LAT Observations of High-Energy γ -Ray Emission Toward the Galactic Center*, *Astrophys. J.* **819** (2016) 44, [[1511.02938](#)].
- [11] C. Karwin, S. Murgia, T. M. P. Tait, T. A. Porter and P. Tanedo, *Dark Matter Interpretation of the Fermi-LAT Observation Toward the Galactic Center*, *Phys. Rev. D* **95** (2017) 103005, [[1612.05687](#)].
- [12] The Fermi-LAT Collaboration, *The Fermi Galactic Center GeV Excess and Implications for Dark Matter*, *ArXiv e-prints* (Apr., 2017) , [[1704.03910](#)].
- [13] S. K. Lee, M. Lisanti, B. R. Safdi, T. R. Slatyer and W. Xue, *Evidence for Unresolved γ -Ray Point Sources in the Inner Galaxy*, *Phys. Rev. Lett.* **116** (Feb., 2016) 051103, [[1506.05124](#)].
- [14] R. Bartels, S. Krishnamurthy and C. Weniger, *Strong Support for the Millisecond Pulsar Origin of the Galactic Center GeV Excess*, *Phys. Rev. Lett.* **116** (Feb., 2016) 051102, [[1506.05104](#)].
- [15] FERMI-LAT collaboration, M. Ajello et al., *Characterizing the population of pulsars in the Galactic bulge with the Fermi Large Area Telescope*, *Submitted to: Astrophys. J.* (2017) , [[1705.00009](#)].
- [16] S. Horiuchi, M. Kaplinghat and A. Kwa, *Investigating the Uniformity of the Excess Gamma rays towards the Galactic Center Region*, *JCAP* **1611** (2016) 053, [[1604.01402](#)].
- [17] K. N. Abazajian, *The Consistency of Fermi-LAT Observations of the Galactic Center with a Millisecond Pulsar Population in the Central Stellar Cluster*, *J. Cosm. & Astropart. Phys.* **1103** (2011) 010, [[1011.4275](#)].
- [18] Q. Yuan and B. Zhang, *Millisecond pulsar interpretation of the Galactic center gamma-ray excess*, *J. High Energy Astrophys.* **3** (Sept., 2014) 1–8, [[1404.2318](#)].
- [19] R. M. O’Leary, M. D. Kistler, M. Kerr and J. Dexter, *Young Pulsars and the Galactic Center GeV Gamma-ray Excess*, *ArXiv e-prints (arXiv:1504.02477)* (Apr., 2015) , [[1504.02477](#)].

- [20] W. Wang, Z. J. Jiang and K. S. Cheng, *Contribution to diffuse gamma-rays in the Galactic Centre region from unresolved millisecond pulsars*, *Mon. Not. R. Astron. Soc.* **358** (Mar., 2005) 263–269, [[astro-ph/0501245](#)].
- [21] T. D. Brandt and B. Kocsis, *Disrupted Globular Clusters Can Explain the Galactic Center Gamma Ray Excess*, *Astrophys. J.* **812** (2015) 15, [[1507.05616](#)].
- [22] O. Y. Gnedin, J. P. Ostriker and S. Tremaine, *Co-evolution of Galactic Nuclei and Globular Cluster Systems*, *ApJ* **785** (Apr., 2014) 71, [[1308.0021](#)].
- [23] F. Camilo and F. A. Rasio, *Pulsars in Globular Clusters*, in *Binary Radio Pulsars* (F. A. Rasio and I. H. Stairs, eds.), vol. 328 of *Astronomical Society of the Pacific Conference Series*, p. 147, July, 2005. [[astro-ph/0501226](#)].
- [24] D. Hooper and T. Linden, *The gamma-ray pulsar population of globular clusters: implications for the GeV excess*, *J. Cosm. & Astropart. Phys.* **8** (Aug., 2016) 018, [[1606.09250](#)].
- [25] D. Hooper and G. Mohlabeng, *The gamma-ray luminosity function of millisecond pulsars and implications for the GeV excess*, *Journal of Cosmology and Astroparticle Physics* **2016** (2016) 049.
- [26] D. Haggard, C. Heinke, D. Hooper and T. Linden, *Low Mass X-Ray Binaries in the Inner Galaxy: Implications for Millisecond Pulsars and the GeV Excess*, [[1701.02726](#)].
- [27] I. Cholis, D. Hooper and T. Linden, *A Critical Reevaluation of Radio Constraints on Annihilating Dark Matter*, *ArXiv e-prints* (Aug., 2014) , [[1408.6224](#)].
- [28] D. Bhattacharya and E. P. J. van den Heuvel, *Formation and evolution of binary and millisecond radio pulsars*, *Physics Rep.* **203** (1991) 1–124.
- [29] N. Ivanova, C. O. Heinke and F. A. Rasio, *Formation of Millisecond Pulsars in Globular Clusters*, in *40 Years of Pulsars: Millisecond Pulsars, Magnetars and More* (C. Bassa, Z. Wang, A. Cumming and V. M. Kaspi, eds.), vol. 983 of *American Institute of Physics Conference Series*, pp. 442–447, Feb., 2008. [[0711.3001](#)]. DOI.
- [30] M. A. Alpar, A. F. Cheng, M. A. Ruderman and J. Shaham, *A new class of radio pulsars*, *Nature* **300** (Dec., 1982) 728–730.
- [31] F. C. Michel, *Origin of millisecond pulsars*, *Nature* **329** (Sept., 1987) 310–312.
- [32] J. E. Grindlay and C. D. Bailyn, *Birth of millisecond pulsars in globular clusters*, *Nature* **336** (Nov., 1988) 48–50.
- [33] L. Ferrario and D. Wickramasinghe, *The birth properties of Galactic millisecond radio pulsars*, *Mon. Not. R. Astron. Soc.* **375** (Mar., 2007) 1009–1016, [[astro-ph/0701444](#)].
- [34] J. R. Hurley, C. A. Tout, D. T. Wickramasinghe, L. Ferrario and P. D. Kiel, *Formation of binary millisecond pulsars by accretion-induced collapse of white dwarfs*, *Mon. Not. R. Astron. Soc.* **402** (Mar., 2010) 1437–1448.
- [35] T. M. Tauris, D. Sanyal, S.-C. Yoon and N. Langer, *Evolution towards and beyond accretion-induced collapse of massive white dwarfs and formation of millisecond pulsars*, *Astron. & Astrophys.* **558** (Oct., 2013) A39, [[1308.4887](#)].
- [36] S. L. Smedley, C. A. Tout, L. Ferrario and D. T. Wickramasinghe, *Formation of redbacks via accretion-induced collapse*, *Mon. Not. R. Astron. Soc.* **446** (Jan., 2015) 2540–2549, [[1410.8352](#)].
- [37] P. Podsiadlowski, N. Langer, A. J. T. Poelarends, S. Rappaport, A. Heger and E. Pfahl, *The Effects of Binary Evolution on the Dynamics of Core Collapse and Neutron Star Kicks*, *ApJ* **612** (Sept., 2004) 1044–1051, [[astro-ph/0309588](#)].
- [38] N. Ivanova, C. O. Heinke, F. A. Rasio, K. Belczynski and J. M. Fregeau, *Formation and evolution of compact binaries in globular clusters - II. Binaries with neutron stars*, *Mon. Not. R. Astron. Soc.* **386** (May, 2008) 553–576, [[0706.4096](#)].

- [39] R.-Z. Yang and F. Aharonian, *On the GeV excess in the diffuse γ -ray emission towards the Galactic centre*, *Astron. & Astrophys.* **589** (May, 2016) A117, [[1602.06764](#)].
- [40] O. Macias, C. Gordon, R. M. Crocker, B. Coleman, D. Paterson, S. Horiuchi et al., *Discovery of Gamma-Ray Emission from the X-shaped Bulge of the Milky Way*, [1611.06644](#).
- [41] S. Konar, *The magnetic fields of millisecond pulsars in globular clusters*, *Mon. Not. R. Astron. Soc.* **409** (Nov., 2010) 259–268, [[1007.1456](#)].
- [42] D. M. Nataf, *The Controversial Star-Formation History and Helium Enrichment of the Milky Way Bulge*, *PASA* **33** (June, 2016) e023, [[1509.00023](#)].
- [43] FERMI-LAT collaboration, F. Acero, M. Ackermann, M. Ajello, A. Albert et al., *Fermi Large Area Telescope Third Source Catalog*, *Astrophys. J. Supp.* **218** (June, 2015) 23, [[1501.02003](#)].
- [44] R. N. Manchester, G. B. Hobbs, A. Teoh and M. Hobbs, *The Australia Telescope National Facility Pulsar Catalogue*, *Astron. J.* **129** (Apr., 2005) 1993–2006, [[astro-ph/0412641](#)].
- [45] C.-A. Faucher-Giguère and A. Loeb, *The Pulsar Contribution to the Gamma-Ray Background*, *JCAP* **1** (2010) 005, [[0904.3102](#)].
- [46] P. G. Mezger, W. J. Duschl and R. Zylka, *The galactic center: a laboratory for agn?*, *The Astronomy and Astrophysics Review* **7** (Dec, 1996) 289–388.
- [47] J. Bland-Hawthorn and O. Gerhard, *The Galaxy in Context: Structural, Kinematic, and Integrated Properties*, *Ann. Rev. Astron. & Astrophys.* **54** (Sept., 2016) 529–596, [[1602.07702](#)].
- [48] FERMI-LAT collaboration, A. Abdo et al., *The Second Fermi Large Area Telescope Catalog of Gamma-ray Pulsars*, *Astrophys. J. Supp.* **208** (2013) 17, [[1305.4385](#)].
- [49] H. Haario, E. Saksman and J. Tamminen, *An adaptive Metropolis algorithm*, *Bernoulli* **7** (2001) 223–242.
- [50] W. Cash, *Parameter estimation in astronomy through application of the likelihood ratio*, *ApJ* **228** (Mar., 1979) 939–947.
- [51] S. A. Story, P. L. Gonthier and A. K. Harding, *Population synthesis of radio and gamma-ray millisecond pulsars from the Galactic disk*, *Astrophys. J.* **671** (2007) 713–726, [[0706.3041](#)].
- [52] T. Grégoire and J. Knödlseider, *Constraining the Galactic millisecond pulsar population using Fermi Large Area Telescope*, *Astron. Astrophys.* **554** (2013) A62, [[1305.1584](#)].
- [53] D. R. Lorimer, *The Galactic Millisecond Pulsar Population*, in *Neutron Stars and Pulsars: Challenges and Opportunities after 80 years* (J. van Leeuwen, ed.), vol. 291 of *IAU Symposium*, pp. 237–242, Mar., 2013. [1210.2746](#). DOI.
- [54] V. Korolev and I. Shevtsova, *An improvement of the berry-esseen inequality with applications to poisson and mixed poisson random sums*, *Scandinavian Actuarial Journal* **2012** (2012) 81–105, [<http://dx.doi.org/10.1080/03461238.2010.485370>].
- [55] A. Gelman, J. Carlin, H. Stern, D. Dunson, A. Vehtari and D. Rubin, *Bayesian Data Analysis*. CRC Press, 3 ed.
- [56] D. Foreman-Mackey, *corner.py: Scatterplot matrices in Python*, *The Journal of Open Source Software* **24** (2016) .
- [57] O. Macias, C. Gordon, R. M. Crocker, B. Coleman, D. Paterson, S. Horiuchi et al. [1611.06644](#).
- [58] Q. Yuan and K. Ioka, *Testing the Millisecond Pulsar Scenario of the Galactic Center Gamma-Ray Excess With Very High Energy Gamma-Rays*, *Astrophys. J.* **802** (Apr., 2015) 124, [[1411.4363](#)].
- [59] L. Levin, M. Bailes, B. R. Barsdell, S. D. Bates, N. D. R. Bhat, M. Burgay et al., *The High Time Resolution Universe Pulsar Survey -VIII. The Galactic millisecond pulsar population*, *Mon. Not. R. Astron. Soc.* **434** (Sept., 2013) 1387–1397, [[1306.4190](#)].
- [60] G. Mohlabeng. Personal communication, Nov., 2016.

- [61] F. Calore, M. Di Mauro, F. Donato, J. W. T. Hessels and C. Weniger, *Radio Detection Prospects for a Bulge Population of Millisecond Pulsars as Suggested by Fermi-LAT Observations of the Inner Galaxy*, *ApJ* **827** (Aug., 2016) 143, [[1512.06825](#)].
- [62] W. H. Press, S. A. Teukolsky, W. T. Vetterling and B. P. Flannery, *Numerical recipes in C++ : the art of scientific computing*. 2002.
- [63] FERMI-LAT collaboration, F. Acero et al. *Astrophys. J. Suppl.* **218** (2015) 23, [[1501.02003](#)].
- [64] J. M. Cordes and T. J. W. Lazio [astro-ph/0207156](#).